

# Neural Moving Horizon Estimation for Robust Flight Control

Bingheng Wang, Zhengtian Ma, Shupeng Lai, and Lin Zhao

**Abstract**—Estimating and reacting to external disturbances is crucial for robust flight control of quadrotors. Existing estimators typically require significant tuning for a specific flight scenario or training with extensive ground-truth disturbance data to achieve satisfactory performance. In this paper, we propose a neural moving horizon estimator (NeuroMHE) that can automatically tune the key parameters modeled by a neural network and adapt to different flight scenarios. We achieve this by deriving the analytical gradients of the MHE estimates with respect to the weighting matrices, which enables a seamless embedding of the MHE as a learnable layer into neural networks for highly effective learning. Interestingly, we show that the gradients can be computed efficiently using a Kalman filter in a recursive form. Moreover, we develop a model-based policy gradient algorithm to train NeuroMHE directly from the quadrotor trajectory tracking error without needing the ground-truth disturbance data. The effectiveness of NeuroMHE is verified extensively via both simulations and physical experiments on quadrotors in various challenging flights. Notably, NeuroMHE outperforms the state-of-the-art neural network based estimator with estimation error reductions of up to about 49.4% by using only a 2.5% amount of the neural network parameters. The proposed method is general and can be applied to robust adaptive control of other robotic systems.

**Index Terms**—Moving horizon estimation, Neural network, Unmanned Aerial Vehicle, Robust control.

## SUPPLEMENTARY MATERIAL

The source code of this work is available at <https://github.com/RCL-NUS/NeuroMHE>.

## I. INTRODUCTION

QUADROTORS have been increasingly engaged in various challenging tasks, such as aerial swarms [1], surveillance [2], aerial manipulation [3], and cooperative transport [4], [5]. They can suffer from strong disturbances caused by capricious wind conditions, unmodeled aerodynamics in extreme flights or tight formations [6]–[10], force interaction with environments, time-varying cable tensions from suspended payloads [11], etc. These disturbances must be compensated appropriately in control systems to avoid significant deterioration in flight performance and even crashing. However, it is generally intractable to have a portable model capable of capturing various disturbances over a wide range of complex flight scenarios. Therefore, online disturbance estimation that adapts to environments is imperative for robust flight control.

The authors are with the Department of Electrical and Computer Engineering, National University of Singapore, 117583 Singapore. wangbingheng@u.nus.edu, shupenglai@gmail.com {zhengtian, elezhli}@nus.edu.sg.

Manuscript received July 11, 2022

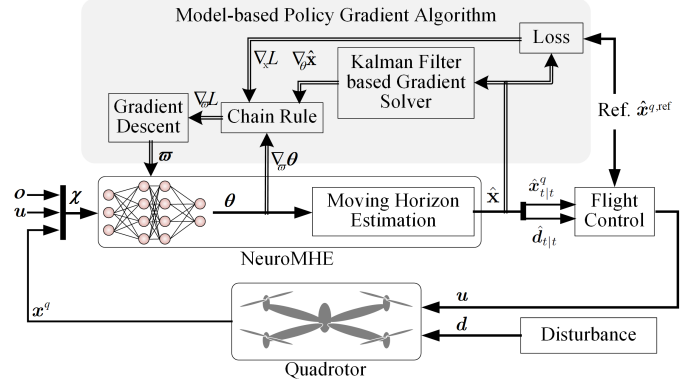


Fig. 1: A diagram of robust flight control system using NeuroMHE and its learning pipelines. We fuse a portable neural network with an MHE to generate adaptive weightings  $\theta$  online. The input of the neural network can be quadrotor state  $x^q$ , control input  $u$ , and other external signals. The neural network parameters  $\varpi$  are learned directly from the trajectory tracking error. Central to our algorithm are the gradients  $\nabla_{\theta} \hat{x}$ , which are calculated recursively using a Kalman filter.

Estimating and reacting to external disturbances has long been a focus of quadrotor research. Some early works [3], [12]–[15] proposed momentum-based estimators using a stable low pass filter. Those methods depend on static disturbance assumption, and thus have limited performance against fast-changing disturbances. McKinnon et al. [16] modelled the dynamics of the disturbances as random walks and applied an unscented Kalman filter (UKF) to estimate the external disturbances. This method generally works well across different scenarios. However, its performance relies heavily on manually tuning tens of noise covariance parameters that are hard to identify. In fact, the tuning process can be rather obscure and requires significant experimental efforts together with much expert knowledge of the overall hardware and software systems. In addition, there has been an increasing interest of utilizing deep neural networks (DNNs) for quadrotor disturbance estimation [10], [11], [17], [18]. Shi et al. [10] trained DNNs to capture the aerodynamic interaction forces between multiple quadrotors in close-proximity flight. Bauersfeld et al. proposed a hybrid estimator NeuroBEM [9] for aerodynamic estimation for a single quadrotor at extreme flight. The latter combines the first-principle Blade Element Momentum model for single rotor aerodynamic modeling and a DNN for residual aerodynamic estimation. These DNN estimators generally employ a relatively large neural network to achieve satisfactory performance. Meanwhile, their training demands significant amounts of ground-truth disturbance data and can require complicated learning curricula.

In this paper, we propose a neural moving horizon estimator (NeuroMHE) that can accurately estimate the external disturbances and adapt to different flight scenarios. Distinct from the aforementioned methods, NeuroMHE fuses a portable neural network with a control-theoretic MHE, which can be trained efficiently without needing the ground-truth disturbance data. MHE solves a nonlinear dynamic optimization online in a receding horizon manner. It is well known to have superior performance on nonlinear systems with uncertainties [19], [20]. The performance of MHE depends on a set of weighting matrices in the cost function. They are roughly inversely proportional to the covariances of the noises that enter the dynamic systems [21]–[24]. However, the tuning of these weightings is difficult in practice due to their large number and strong coupling, as well as the nonlinearity of the system dynamics. It becomes even more challenging when the optimal weightings are dynamic and highly nonlinear in reality. For example, this is the case when the noise covariances are functions of states or some external signals [25]–[27]. In NeuroMHE, we employ a portable neural network to generate adaptive weightings and develop a systematic way to tune these weightings online using machine learning techniques. Our approach leverages the advantages of both model-free and model-based methods—the expressive power of neural networks and the control-theoretic optimal estimation. Such a fusion provides NeuroMHE with high estimation accuracy for various external disturbances and fast online environment adaption.

Fig. 1 outlines the robust flight control system using NeuroMHE and its learning pipelines. The estimated disturbance forces and torques (denoted by  $\hat{d}_{t|t}$  in the figure) from the NeuroMHE will be compensated in the flight controller. We develop a model-based policy gradient algorithm (the shaded blocks) to train the neural network parameters directly from the quadrotor trajectory tracking error. One of the key ingredients of the algorithm is the computation of the gradients of the MHE estimates with respect to the weightings. They are derived by implicitly differentiating through the Karush-Kuhn-Tucker (KKT) conditions of the corresponding MHE optimization problem. In particular, we derive a Kalman filter to compute these gradients very efficiently in a recursive form. These analytical gradients enable a seamless embedding of the MHE as a learnable layer into the neural network for highly effective learning. They allow for training NeuroMHE with powerful machine learning tools.

There has been a growing interest in joining the force of control-theoretic policies and machine learning approaches, such as OptNet [28], differentiable MPC [29], and Pontryagin differentiable programming [30], [31]. Our work adds to this collection another general policy for estimation, which is of interdisciplinary interest to both robotics and machine learning communities. Other recent works on optimally tuning MHE using gradient descent include [32], [33]. There the gradients are computed via solving the inverse of a large KKT matrix, whose size is linear with respect to the MHE horizon. The computational complexity is at least quadratic with respect to the horizon. Besides, the method in [33] requires the system dynamics to be linear. In comparison, our proposed

algorithm of computing the gradients explores a recursive form using a Kalman filter, which has a linear computational complexity with respect to the MHE horizon. Moreover, it directly handles general nonlinear dynamic systems, which has more applications in robotics.

We validate the effectiveness of NeuroMHE extensively via both simulations and physical experiments on quadrotors in various challenging flights. Using the real agile and extreme flight dataset collected in the world’s largest indoor motion capture room [9], we show that compared with the state-of-the-art estimator NeuroBEM, our method: 1) requires much less training data; 2) uses a mere 2.5% amount of the neural network parameters; and 3) achieves superior performance with force estimation error reductions of up to 49.4%. Further utilizing a trajectory tracking simulation with synthetic disturbances, we show that a stable NeuroMHE with a fast dynamic response can be efficiently trained in merely a few episodes from the trajectory tracking error. Beyond the impressive training efficiency, this simulation also demonstrates the robust control performance of using NeuroMHE under Gaussian noises with dynamic covariances. As compared to fixed-weighting MHE, NeuroMHE reduces the average tracking errors by up to 42%. Finally, we conduct experiments to show that NeuroMHE robustifies a baseline flight controller substantially against challenging disturbances, including sudden payload change and counteracting the downwash flow.

This paper is based on our previous conference paper [34]. The earlier version of this work proposed an auto-tuning MHE algorithm with analytical gradients, and demonstrated training of fixed-weighting MHE to achieve quadrotor robust control in simulation. In this work, we additionally: 1) propose a more powerful auto-tuning NeuroMHE, to further improve the estimation accuracy and achieve fast online adaptation; 2) provide theoretical justification of the computational efficiency of the Kalman filter based gradient solver; 3) extend the theory and algorithms to consider constraints in the estimation, which is more practical; 4) conduct extensive simulations using both real and synthetic data to demonstrate the training efficiency, fast environment adaptation, and the improved estimation accuracy over the state-of-the-art estimator; and 5) further test the proposed algorithm on a real quadrotor to show that NeuroMHE can significantly robustify a flight controller against various challenging disturbances.

The rest of this paper is organized as follows. Section II briefly reviews the quadrotor dynamics and the MHE problem for the disturbance estimation. Section III formulates NeuroMHE. In Section IV, we derive the analytical gradients via a sensitivity analysis. Section V develops the model-based policy gradient algorithm for training NeuroMHE without the need for the ground-truth data. Section VI considers constrained NeuroMHE problems. Simulation and experiment results are reported in Section VII. We conclude this paper and discuss our future work in Section VIII.

## II. PRELIMINARIES

### A. Quadrotor and Disturbance Dynamics

We model a quadrotor as a 6 degree-of-freedom (DoF) rigid body with mass  $m$  and moment of inertia  $\mathbf{J} \in \mathbb{R}^{3 \times 3}$ . Let

$\mathbf{p} \in \mathbb{R}^3$  denote the global position of Center-of-Mass (CoM) in world frame  $\mathcal{I}$ ,  $\mathbf{v} \in \mathbb{R}^3$  the velocity of CoM in  $\mathcal{I}$ ,  $\mathbf{R} \in SO(3)$  the rotation matrix from body frame  $\mathcal{B}$  to  $\mathcal{I}$ , and  $\boldsymbol{\omega} \in \mathbb{R}^3$  the angular velocity in  $\mathcal{B}$ . The quadrotor model is given by:

$$\dot{\mathbf{p}} = \mathbf{v}, \quad \dot{\mathbf{v}} = m^{-1}(-mg\mathbf{z} + \mathbf{R}\mathbf{f}\mathbf{z} + \mathbf{d}_f), \quad (1a)$$

$$\dot{\mathbf{R}} = \mathbf{R}\boldsymbol{\omega}^\times, \quad \dot{\boldsymbol{\omega}} = \mathbf{J}^{-1}(-\boldsymbol{\omega}^\times \mathbf{J}\boldsymbol{\omega} + \boldsymbol{\tau}_m + \mathbf{d}_\tau), \quad (1b)$$

where the disturbance forces  $\mathbf{d}_f = [d_{fx}; d_{fy}; d_{fz}]$  and torques  $\mathbf{d}_\tau = [d_{\tau x}; d_{\tau y}; d_{\tau z}]$  are expressed in  $\mathcal{I}$  and  $\mathcal{B}$ , respectively,  $g$  is the gravitational acceleration,  $\mathbf{z} = [0; 0; 1]$ ,  $\boldsymbol{\omega}^\times$  denotes the skew-symmetric matrix form of  $\boldsymbol{\omega}$  as an element of the Lie algebra  $so(3)$ , and  $\mathbf{f}$  and  $\boldsymbol{\tau}_m = [\tau_{mx}; \tau_{my}; \tau_{mz}]$  are the total thrust and control torques produced by the quadrotor's four motors, respectively. We define  $\mathbf{x}^q = [\mathbf{p}; \mathbf{v}; \text{vec}(\mathbf{R}); \boldsymbol{\omega}]$  as the quadrotor state where  $\text{vec}(\cdot)$  denotes the vectorization of a given matrix and  $\mathbf{u} = [f; \tau_{mx}; \tau_{my}; \tau_{mz}]$  as the control input.

The disturbance can come from various sources (e.g., aerodynamic drag or tension force from cable-suspended payloads). A general way to model its dynamics is using random walks:

$$\dot{\mathbf{d}}_f = \mathbf{w}_f, \quad \dot{\mathbf{d}}_\tau = \mathbf{w}_\tau, \quad (2)$$

where  $\mathbf{w}_f \in \mathbb{R}^3$  and  $\mathbf{w}_\tau \in \mathbb{R}^3$  are the process noises. This model has been proven very efficient in estimation of unknown and time-varying disturbances [16]. Augmenting the quadrotor state  $\mathbf{x}^q$  with the disturbance state  $\mathbf{d} = [\mathbf{d}_f; \mathbf{d}_\tau]$ , we define the augmented state  $\mathbf{x} = [\mathbf{p}; \mathbf{v}; \mathbf{d}_f; \text{vec}(\mathbf{R}); \boldsymbol{\omega}; \mathbf{d}_\tau]$ . The overall dynamics model can be written as:

$$\dot{\mathbf{x}} = \mathbf{f}_{\text{dyn}}(\mathbf{x}, \mathbf{u}, \mathbf{w}), \quad (3a)$$

$$\mathbf{y} = \mathbf{h}(\mathbf{x}) + \boldsymbol{\nu}, \quad (3b)$$

where  $\mathbf{f}_{\text{dyn}}$  consists of both the quadrotor rigid body dynamics (1) and the disturbance model (2),  $\mathbf{w} = [\mathbf{w}_f; \mathbf{w}_\tau]$  is the process noise vector,  $\mathbf{h}$  is the measurement function, and  $\mathbf{y}$  is the measurement subject to the noise  $\boldsymbol{\nu}$ . The model (3) will be used in MHE for estimation.

### B. Moving Horizon Estimator

MHE is a control-theoretic estimator which solves a nonlinear dynamic optimization online in a receding horizon manner. At time step  $t = N, N+1, \dots$ , the MHE estimator optimizes over  $N+1$  state vectors  $\mathbf{x} = \{\mathbf{x}_k\}_{k=t-N}^t$  and  $N$  process noise vectors  $\mathbf{w} = \{\mathbf{w}_k\}_{k=t-N}^{t-1}$  on the basis of  $N+1$  measurements  $\{\mathbf{y}_k\}_{k=t-N}^t$  and  $N$  control inputs  $\{\mathbf{u}_k\}_{k=t-N}^{t-1}$  collected in a sliding window of length  $N$ . We denote by  $\hat{\mathbf{x}} = \{\hat{\mathbf{x}}_{k|t}\}_{k=t-N}^t$  and  $\hat{\mathbf{w}} = \{\hat{\mathbf{w}}_{k|t}\}_{k=t-N}^{t-1}$  the MHE estimates of  $\mathbf{x}$  and  $\mathbf{w}$ ,

respectively at time step  $t$ . They are the solutions of the following optimization problem:

$$\begin{aligned} \min_{\mathbf{x}, \mathbf{w}} J := & \underbrace{\frac{1}{2} \|\mathbf{x}_{t-N} - \hat{\mathbf{x}}_{t-N}\|_{\mathbf{P}}^2}_{\text{arrival cost}} \\ & + \underbrace{\frac{1}{2} \sum_{k=t-N}^t \|\mathbf{y}_k - \mathbf{h}(\mathbf{x}_k)\|_{\mathbf{R}_k}^2 + \frac{1}{2} \sum_{k=t-N}^{t-1} \|\mathbf{w}_k\|_{\mathbf{Q}_k}^2}_{\text{running cost}} \end{aligned} \quad (4a)$$

$$\text{s.t. } \mathbf{x}_{k+1} = \mathbf{f}(\mathbf{x}_k, \mathbf{u}_k, \mathbf{w}_k, \Delta t), \quad (4b)$$

where all the norms are 2-norms weighted by the positive definite matrices  $\mathbf{P}$ ,  $\mathbf{R}_k$ , and  $\mathbf{Q}_k$ , e.g.,  $\|\mathbf{w}_k\|_{\mathbf{Q}_k}^2 = \mathbf{w}_k^T \mathbf{Q}_k \mathbf{w}_k$ ,  $\Delta t$  is the sampling time,  $\mathbf{f}(\mathbf{x}_k, \mathbf{u}_k, \mathbf{w}_k, \Delta t)$  is the discrete-time model of  $\mathbf{f}_{\text{dyn}}$  for predicting the state, and  $\hat{\mathbf{x}}_{t-N}$  is the filter priori [35] which is chosen as the MHE estimate  $\hat{\mathbf{x}}_{t-N|t-1}$  of  $\mathbf{x}_{t-N}$  obtained at  $t-1$ . The first term of (4a) is referred to as the arrival cost, which summarizes the historical running cost before the current estimation horizon [36]. The second and third terms of (4a) are the running cost, which minimize the predicted measurement error and state error.

## III. FORMULATION OF NEUROMHE

### A. Problem Statement

The MHE performance depends on the choice of the weighting matrices. Their tuning typically requires the priori knowledge of the covariances of the noises that enter the dynamic systems. For example, the higher the covariance is, the lower confidence we have in the polluted data. Then the weighting should be set lower on minimizing the predicted estimation error in the running cost. Despite these rough intuitions, the tuning of the weighting matrices is still demanding due to their large number and complex coupling. It becomes even more challenging when the optimal weightings are dynamic in reality.

For the ease of presentation, we represent all the weighting matrices as  $\boldsymbol{\theta}$ , parameterize Problem (4) as MHE( $\boldsymbol{\theta}$ ), and denote the corresponding MHE estimates by  $\hat{\mathbf{x}}(\boldsymbol{\theta})$ . If the ground-truth system state is available, we can directly evaluate the estimation quality using a differentiable scalar loss function  $L(\hat{\mathbf{x}}(\boldsymbol{\theta}))$  built upon the estimation error. Probably more meaningful in robust trajectory tracking control,  $L(\hat{\mathbf{x}}(\boldsymbol{\theta}))$  can be chosen to penalize the tracking error. Thus, the tuning problem is to find optimal weightings  $\boldsymbol{\theta}^*$  such that the tracking error loss is minimized. It can be interpreted as the following optimization problem:

$$\min_{\boldsymbol{\theta}} L(\hat{\mathbf{x}}(\boldsymbol{\theta})) \quad (5a)$$

$$\text{s.t. } \hat{\mathbf{x}}(\boldsymbol{\theta}) \text{ generated by MHE}(\boldsymbol{\theta}). \quad (5b)$$

Traditionally, a fixed  $\boldsymbol{\theta}^*$  is tuned for the vanilla MHE, which may not be optimal and can have substantially degraded performance when the noise covariances are dynamic. Therefore, we are interested in modeling an adaptive  $\boldsymbol{\theta}^*$  to improve the estimation or control performance.

### B. Neural MHE Adaptive Weightings

The adaptive weightings are generally difficult to model using the first principle. Instead, we employ a neural network to approximate them, denoted by

$$\theta = f_{\varpi}(\chi), \quad (6)$$

where  $\varpi$  denote the neural network parameters, and the input  $\chi$  can be various signals such as quadrotor state  $x^q$ , control input  $u$ , or other external signals, depending on the priori knowledge and applications.

### C. Tuning NeuroMHE via Gradient Descent

For NeuroMHE, the tuning becomes finding the optimal neural network parameters  $\varpi^*$  to minimize the loss function, that is,

$$\min_{\varpi} L(\hat{x}(\varpi)) \quad (7a)$$

$$\text{s.t. } \hat{x}(\varpi) \text{ generated by NeuroMHE}(\theta(\varpi)). \quad (7b)$$

Compared with the fixed  $\theta^*$  employed in (5), the neural network parameterized  $\theta^*(\varpi^*)$  is more powerful, which varies according to different states or external signals  $\chi$ , thus allowing for fast online adaptation to different flight status and scenarios.

We aim to use gradient descent to train  $\varpi$ . The gradient of  $L(\hat{x}(\varpi))$  with respect to  $\varpi$  can be calculated using the chain rule

$$\frac{dL(\hat{x}(\varpi))}{d\varpi} = \frac{\partial L(\hat{x})}{\partial \hat{x}} \frac{\partial \hat{x}(\theta)}{\partial \theta} \frac{\partial \theta(\varpi)}{\partial \varpi}. \quad (8)$$

Fig. 1 depicts the learning pipelines for training NeuroMHE. Each update of  $\varpi$  consists of a *forward pass* and a *backward pass*. In the forward pass, given the current  $\varpi_t$ , the weightings  $\theta_t$  are generated from the neural network for MHE to obtain  $\hat{x}$ , and thus  $L(\hat{x}(\varpi_t))$  is evaluated. In the backward pass, the gradients components  $\frac{\partial L(\hat{x})}{\partial \hat{x}}$ ,  $\frac{\partial \hat{x}(\theta)}{\partial \theta}$ , and  $\frac{\partial \theta(\varpi)}{\partial \varpi}$  are computed.

In solving the MHE,  $\hat{x}$  can be obtained by any numerical optimization solver. In the backward pass, the gradient  $\frac{\partial L(\hat{x})}{\partial \hat{x}}$  is straightforward to compute as  $L(\hat{x})$  is generally an explicit function of  $\hat{x}$ ; computing  $\frac{\partial \theta(\varpi)}{\partial \varpi}$  for the neural network is standard and handy via many existing machine learning tools. The main challenge is how to solve for  $\frac{\partial \hat{x}(\theta)}{\partial \theta}$ , the gradients of the MHE estimates with respect to  $\theta$ . This requires differentiating through the MHE problem (4) which is a nonlinear optimization. Next, we will derive  $\frac{\partial \hat{x}(\theta)}{\partial \theta}$  analytically and show that it can be computed recursively using a Kalman filter.

## IV. ANALYTICAL GRADIENTS

The idea to derive  $\frac{\partial \hat{x}}{\partial \theta}$  is to implicitly differentiate through the KKT conditions associated with the MHE problem (4). The KKT conditions define a set of first-order optimality conditions which the locally optimal  $\hat{x}$  must satisfy. We associate the equality constraints (4b) with the dual variables  $\lambda = \{\lambda_k\}_{k=t-N}^{t-1}$  and denote their optimal values by  $\lambda^*$ . Then, the corresponding Lagrangian can be written as

$$\mathcal{L} = \frac{1}{2} \|x_{t-N} - \hat{x}_{t-N}\|_P^2 + \bar{\mathcal{L}}, \quad (9)$$

where

$$\begin{aligned} \bar{\mathcal{L}} = & \frac{1}{2} \sum_{k=t-N}^t \|y_k - h(x_k)\|_{R_k}^2 + \frac{1}{2} \sum_{k=t-N}^{t-1} \|w_k\|_{Q_k}^2 \\ & + \sum_{k=t-N}^{t-1} \lambda_k^T (x_{k+1} - f(x_k, u_k, w_k, \Delta t)). \end{aligned}$$

Then the KKT conditions of (4) at  $\hat{x}$ ,  $\hat{w}$ , and  $\lambda^*$  are given by

$$\begin{aligned} \nabla_{x_{t-N}} \mathcal{L} = & P(\hat{x}_{t-N|t} - \hat{x}_{t-N}) \\ & - H_{t-N}^T R_{t-N} (y_{t-N} - h(\hat{x}_{t-N|t})) \\ & - F_{t-N}^T \lambda_{t-N}^* = 0, \end{aligned} \quad (10a)$$

$$\begin{aligned} \nabla_{x_k} \mathcal{L} = & \lambda_{k-1}^* - H_k^T R_k (y_k - h(\hat{x}_{k|t})) \\ & - F_k^T \lambda_k^* = 0, \quad k = t-N+1, \dots, t, \end{aligned} \quad (10b)$$

$$\begin{aligned} \nabla_{w_k} \mathcal{L} = & Q_k \hat{w}_{k|t} - G_k^T \lambda_k^* = 0, \\ & k = t-N, \dots, t-1, \end{aligned} \quad (10c)$$

$$\begin{aligned} \nabla_{\lambda_k} \mathcal{L} = & \hat{x}_{k+1|t} - f(\hat{x}_{k|t}, u_k, \hat{w}_{k|t}, \Delta t) = 0, \\ & k = t-N, \dots, t-1, \end{aligned} \quad (10d)$$

where

$$F_k = \frac{\partial f}{\partial \hat{x}_{k|t}}, \quad G_k = \frac{\partial f}{\partial \hat{w}_{k|t}}, \quad H_k = \frac{\partial h}{\partial \hat{x}_{k|t}}, \quad (11)$$

and  $\lambda_t^* = 0$  by definition.

### A. Differential KKT Conditions of MHE

Recall that

$$\frac{\partial \hat{x}}{\partial \theta} = \left\{ \frac{\partial \hat{x}_{k|t}}{\partial \theta} \right\}_{k=t-N}^t, \quad (12)$$

and therefore, we are motivated to implicitly differentiate the KKT conditions (10) on both sides with respect to  $\theta$ . This results in the following *differential* KKT conditions.

$$\begin{aligned} \frac{d\nabla_{x_{t-N}} \mathcal{L}}{d\theta} = & L_{t-N}^{xx} \frac{\partial \hat{x}_{t-N|t}}{\partial \theta} - P \frac{\partial \hat{x}_{t-N}}{\partial \theta} + L_{t-N}^{x\theta} \\ & + L_{t-N}^{xw} \frac{\partial \hat{w}_{t-N|t}}{\partial \theta} - F_{t-N}^T \frac{\partial \lambda_{t-N}^*}{\partial \theta} = 0, \end{aligned} \quad (13a)$$

$$\begin{aligned} \frac{d\nabla_{x_k} \mathcal{L}}{d\theta} = & L_k^{xx} \frac{\partial \hat{x}_{k|t}}{\partial \theta} + L_k^{xw} \frac{\partial \hat{w}_{k|t}}{\partial \theta} - F_k^T \frac{\partial \lambda_k^*}{\partial \theta} \\ & + \frac{\partial \lambda_{k-1}^*}{\partial \theta} + L_k^{x\theta} = 0, \\ & k = t-N+1, \dots, t, \end{aligned} \quad (13b)$$

$$\begin{aligned} \frac{d\nabla_{w_k} \mathcal{L}}{d\theta} = & L_k^{wx} \frac{\partial \hat{x}_{k|t}}{\partial \theta} + L_k^{ww} \frac{\partial \hat{w}_{k|t}}{\partial \theta} - G_k^T \frac{\partial \lambda_k^*}{\partial \theta} \\ & + L_k^{w\theta} = 0, \quad k = t-N, \dots, t-1, \end{aligned} \quad (13c)$$

$$\begin{aligned} \frac{d\nabla_{\lambda_k} \mathcal{L}}{d\theta} = & \frac{\partial \hat{x}_{k+1|t}}{\partial \theta} - F_k \frac{\partial \hat{x}_{k|t}}{\partial \theta} - G_k \frac{\partial \hat{w}_{k|t}}{\partial \theta} = 0, \\ & k = t-N, \dots, t-1, \end{aligned} \quad (13d)$$

where the coefficient matrices are defined as follows:

$$L_k^{xx} = \frac{\partial^2 \mathcal{L}}{\partial \hat{x}_{k|t}^2}, \quad L_k^{xw} = \frac{\partial^2 \mathcal{L}}{\partial \hat{x}_{k|t} \partial \hat{w}_{k|t}}, \quad L_k^{x\theta} = \frac{\partial^2 \mathcal{L}}{\partial \hat{x}_{k|t} \partial \theta}, \quad (14a)$$

$$L_k^{wx} = \frac{\partial^2 \mathcal{L}}{\partial \hat{w}_{k|t} \partial \hat{x}_{k|t}}, \quad L_k^{ww} = \frac{\partial^2 \mathcal{L}}{\partial \hat{w}_{k|t} \partial \hat{w}_{k|t}}, \quad L_k^{w\theta} = \frac{\partial^2 \mathcal{L}}{\partial \hat{w}_{k|t} \partial \theta}, \quad (14b)$$

for  $k = t - N, \dots, t$ . In (13a) and (13b),  $\frac{\partial \mathbf{y}_{t-N}}{\partial \boldsymbol{\theta}}$  and  $\frac{\partial \mathbf{y}_k}{\partial \boldsymbol{\theta}}$  are zeros as the measurements are independent of  $\boldsymbol{\theta}$ . The analytical expressions of all the matrices defined in (11) and (14) can be obtained via any software package that supports symbolic computation (e.g., CasADi [37]), and their values are known from the trajectories  $\hat{\mathbf{x}}$ ,  $\hat{\mathbf{w}}$ , and  $\boldsymbol{\lambda}^*$  obtained in the forward pass. Note that  $\frac{\partial \hat{\mathbf{x}}_{t-N}}{\partial \boldsymbol{\theta}}$  is also known since by choice it is equal to  $\frac{\partial \hat{\mathbf{x}}_{t-N|t-1}}{\partial \boldsymbol{\theta}}$  which is obtained at the previous time step  $t - 1$ . We denote  $\frac{\partial \hat{\mathbf{x}}_{t-N}}{\partial \boldsymbol{\theta}}$  by  $\hat{\mathbf{X}}_{t-N}$  to distinguish it from the unknown matrices  $\left\{ \frac{\partial \hat{\mathbf{x}}_{k|t}}{\partial \boldsymbol{\theta}} \right\}_{k=t-N}^t$ ,  $\left\{ \frac{\partial \hat{\mathbf{w}}_{k|t}}{\partial \boldsymbol{\theta}} \right\}_{k=t-N}^{t-1}$ , and  $\left\{ \frac{\partial \boldsymbol{\lambda}_k^*}{\partial \boldsymbol{\theta}} \right\}_{k=t-N}^{t-1}$ . Next, we will demonstrate that these unknowns can be computed recursively by the Kalman filter-based solver proposed in the following subsection.

### B. Kalman Filter-based Gradient Solver

From the definitions in (14), we can further calculate that  $\mathbf{L}_{t-N}^{xx} = \mathbf{P} + \bar{\mathbf{L}}_{t-N}^{xx}$ , where  $\bar{\mathbf{L}}_{t-N}^{xx} = \frac{\partial^2 \bar{\mathcal{L}}}{\partial \hat{\mathbf{x}}_{t-N|t}^2}$ . Plugging it back to (13a), we can see that the differential KKT conditions (13) have the similar structure to the original KKT conditions (10). More importantly, it can be interpreted as the KKT conditions of an auxiliary MHE system whose optimal state estimates are exactly the gradients (12). To formalize it, we define the new state estimate, process noise estimate, and optimal dual variable of the auxiliary MHE as

$$\hat{\mathbf{X}}_{k|t} = \frac{\partial \hat{\mathbf{x}}_{k|t}}{\partial \boldsymbol{\theta}}, \quad \hat{\mathbf{W}}_{k|t} = \frac{\partial \hat{\mathbf{w}}_{k|t}}{\partial \boldsymbol{\theta}}, \quad \boldsymbol{\Lambda}_k^* = \frac{\partial \boldsymbol{\lambda}_k^*}{\partial \boldsymbol{\theta}}, \quad (15)$$

respectively, and formulate the auxiliary MHE system in the following lemma.

**Lemma 1.** Let  $\hat{\mathbf{X}} = \left\{ \hat{\mathbf{X}}_{k|t} \right\}_{k=t-N}^t$  and  $\hat{\mathbf{W}} = \left\{ \hat{\mathbf{W}}_{k|t} \right\}_{k=t-N}^{t-1}$  be the optimal estimates of the following auxiliary MHE system:

$$\begin{aligned} \min_{\hat{\mathbf{X}}, \hat{\mathbf{W}}} J_2 := & \frac{1}{2} \text{Tr} \left\| \mathbf{X}_{t-N|t} - \hat{\mathbf{X}}_{t-N} \right\|_{\mathbf{P}}^2 \\ & + \text{Tr} \sum_{k=t-N}^t \left( \frac{1}{2} \mathbf{X}_k^T \bar{\mathbf{L}}_k^{xx} \mathbf{X}_k + \mathbf{W}_k^T \mathbf{L}_k^{wx} \mathbf{X}_k \right) \\ & + \text{Tr} \sum_{k=t-N}^{t-1} \left( \frac{1}{2} \mathbf{W}_k^T \mathbf{L}_k^{ww} \mathbf{W}_k + (\mathbf{L}_k^{w\theta})^T \mathbf{W}_k \right) \\ & + \text{Tr} \sum_{k=t-N}^t \left( (\mathbf{L}_k^{x\theta})^T \mathbf{X}_k \right) \end{aligned} \quad (16a)$$

$$\text{s.t. } \mathbf{X}_{k+1} = \mathbf{F}_k \mathbf{X}_k + \mathbf{G}_k \mathbf{W}_k, \quad (16b)$$

where  $\bar{\mathbf{L}}_k^{xx} = \mathbf{L}_k^{xx}$  for  $k = t - N + 1, \dots, t$  and  $\text{Tr}(\cdot)$  takes the trace of a given matrix. Then, they satisfy the differential KKT conditions (13).

The proof of Lemma 1 can be found in Appendix-A. This lemma shows that the KKT conditions of (16) are the same as the differential KKT conditions (13) of the original MHE problem (4). In particular, the solution  $\hat{\mathbf{X}}$  of (16) are exactly the gradients of  $\hat{\mathbf{x}}$  with respect to  $\boldsymbol{\theta}$ . Hence, we can compute

the desired gradients (12) by solving the auxiliary MHE system (16). Notice that for this auxiliary MHE, its cost function (16a) is quadratic and the dynamics model (16b) is linear. Therefore, it is possible to obtain  $\hat{\mathbf{X}}$  in a closed form. Instead of solving the auxiliary MHE by some numerical optimization solver, we propose a computationally more efficient method to recursively solve for  $\hat{\mathbf{X}}$  using a Kalman filter. We now present the key result in the following lemma, which is obtained using forward dynamic programming [38].

**Lemma 2.** Given the initial conditions

$$\hat{\mathbf{X}}_{t-N|t-N}^{\text{KF}} = (\mathbf{I} + \mathbf{C}_{t-N} \mathbf{S}_{t-N}) \bar{\mathbf{X}}_{t-N}, \quad (17a)$$

$$\mathbf{C}_{t-N} = (\mathbf{I} - \mathbf{P}_{t-N} \mathbf{S}_{t-N})^{-1} \mathbf{P}_{t-N}, \quad (17b)$$

where  $\mathbf{I}$  is an identity matrix,  $\bar{\mathbf{X}}_{t-N} = \mathbf{P}_{t-N} \mathbf{T}_{t-N} + \hat{\mathbf{X}}_{t-N}$ ,  $\mathbf{P}_{t-N} = \mathbf{P}^{-1}$ ,  $\mathbf{S}_{t-N} = \mathbf{L}_{t-N}^{xw} (\mathbf{L}_{t-N}^{ww})^{-1} \mathbf{L}_{t-N}^{wx} - \bar{\mathbf{L}}_{t-N}^{xx}$ , and  $\mathbf{T}_{t-N} = \mathbf{L}_{t-N}^{xw} (\mathbf{L}_{t-N}^{ww})^{-1} \mathbf{L}_{t-N}^{w\theta} - \mathbf{L}_{t-N}^{x\theta}$ , the optimal estimates  $\hat{\mathbf{X}}$  of the auxiliary MHE (16) can be obtained recursively through the following steps.

First, a Kalman filter (KF) is solved for  $k = t - N + 1, \dots, t$  to generate  $\left\{ \hat{\mathbf{X}}_{k|k}^{\text{KF}} \right\}_{k=t-N+1}^t$  and  $\left\{ \mathbf{C}_k \right\}_{k=t-N+1}^t$ :

$$\hat{\mathbf{X}}_{k|k-1} = \bar{\mathbf{F}}_{k-1} \hat{\mathbf{X}}_{k-1|k-1}^{\text{KF}} - \mathbf{G}_{k-1} (\mathbf{L}_{k-1}^{ww})^{-1} \mathbf{L}_{k-1}^{w\theta}, \quad (18a)$$

$$\mathbf{P}_k = \bar{\mathbf{F}}_{k-1} \mathbf{C}_{k-1} \bar{\mathbf{F}}_{k-1}^T + \mathbf{G}_{k-1} (\mathbf{L}_{k-1}^{ww})^{-1} \mathbf{G}_{k-1}^T, \quad (18b)$$

$$\mathbf{C}_k = (\mathbf{I} - \mathbf{P}_k \mathbf{S}_k)^{-1} \mathbf{P}_k, \quad (18c)$$

$$\hat{\mathbf{X}}_{k|k}^{\text{KF}} = (\mathbf{I} + \mathbf{C}_k \mathbf{S}_k) \hat{\mathbf{X}}_{k|k-1} + \mathbf{C}_k \mathbf{T}_k, \quad (18d)$$

where for  $k = t - N + 1, \dots, t - 1$ ,  $\bar{\mathbf{F}}_k = \mathbf{F}_k - \mathbf{G}_k (\mathbf{L}_k^{ww})^{-1} \mathbf{L}_k^{wx}$ ,  $\mathbf{S}_k = \mathbf{L}_k^{xw} (\mathbf{L}_k^{ww})^{-1} \mathbf{L}_k^{wx} - \bar{\mathbf{L}}_k^{xx}$ ,  $\mathbf{T}_k = \mathbf{L}_k^{xw} (\mathbf{L}_k^{ww})^{-1} \mathbf{L}_k^{w\theta} - \mathbf{L}_k^{x\theta}$ , when  $k = t$ , then  $\mathbf{S}_t = -\bar{\mathbf{L}}_t^{xx}$ , and  $\mathbf{T}_t = -\mathbf{L}_t^{x\theta}$ .

Second,  $\boldsymbol{\Lambda}^* = \left\{ \boldsymbol{\Lambda}_k^* \right\}_{k=t-N}^{t-1}$  are generated by solving the following equation backward in time for  $k = t, \dots, t - N + 1$ , starting with  $\boldsymbol{\Lambda}_t^* = \mathbf{0}$ :

$$\boldsymbol{\Lambda}_{k-1}^* = (\mathbf{I} + \mathbf{S}_k \mathbf{C}_k) \bar{\mathbf{F}}_k^T \boldsymbol{\Lambda}_k^* + \mathbf{S}_k \hat{\mathbf{X}}_{k|k}^{\text{KF}} + \mathbf{T}_k. \quad (19)$$

Finally,  $\hat{\mathbf{X}}$  are obtained by solving

$$\hat{\mathbf{X}}_{k|t} = \hat{\mathbf{X}}_{k|k}^{\text{KF}} + \mathbf{C}_k \bar{\mathbf{F}}_k^T \boldsymbol{\Lambda}_k^* \quad (20)$$

forward in time for  $k = t - N, \dots, t$ .

The proof is presented in Appendix-B. Equations in (18) represent a Kalman filter with the matrix state  $\hat{\mathbf{X}}_{k|k}^{\text{KF}}$  and "zero measurement" (due to  $\frac{\partial \mathbf{y}_k}{\partial \boldsymbol{\theta}} = \mathbf{0}$ ). Among them, (18a) is the state predictor, (18b) is the projection of the error covariance, (18c) is the update of the error covariance from which the Kalman gain can be obtained using the matrix inversion lemma, and (18d) is the state corrector. The Kalman filter provides the analytical gradients in a recursive form, making their computation very efficient. This algorithm acts as a key component in the backward pass of training NeuroMHE, as shown in Fig. 1. We summarize the procedure of solving for  $\hat{\mathbf{X}}$  using a Kalman filter in Algorithm 1.

**Algorithm 1:** Solving for  $\hat{\mathbf{X}}$  using a Kalman Filter

---

**Input:** The trajectories  $\hat{\mathbf{x}}$ ,  $\hat{\mathbf{w}}$ , and  $\boldsymbol{\Lambda}^*$  generated by solving the MHE problem (4), the current weightings  $\boldsymbol{\theta}$ , the trajectory of the control input  $\mathbf{u}$ , the gradient of the filter priori  $\hat{\mathbf{X}}_{t-N}$ , and the matrices in (11) and (14) for constructing the auxiliary MHE system (16);

```

1  def Kalman_Filter_based_Gradient_Solver:
2      ▷ implementation of Lemma 2
3      Set  $\hat{\mathbf{X}}_{t-N|t-N}^{\text{KF}}$  and  $\mathbf{C}_{t-N}$  using equation (17);
4      for  $k \leftarrow t - N + 1$  to  $t$  do
5          ▷ Kalman Filter
6          Update  $\mathbf{C}_k$  and  $\hat{\mathbf{X}}_{k|k}^{\text{KF}}$  using equation (18);
          ▷ forward recursion
7      end for
8      Set  $\boldsymbol{\Lambda}_t^* = \mathbf{0}$ ;
9      for  $k \leftarrow t$  to  $t - N + 1$  do
10         Update  $\boldsymbol{\Lambda}_{k-1}^*$  using equation (19);
         ▷ backward recursion
11     end for
12     for  $k \leftarrow t - N$  to  $t$  do
13         Update  $\hat{\mathbf{X}}_{k|t}$  using equation (20);
         ▷ forward recursion
14     end for
15 return  $\left\{ \hat{\mathbf{X}}_{k|t} \right\}_{k=t-N}^t$ 

```

**Return:**  $\frac{\partial \hat{\mathbf{x}}}{\partial \boldsymbol{\theta}} = \hat{\mathbf{X}}$  ▷ due to Lemma 1

---

## V. MODEL-BASED POLICY GRADIENT ALGORITHM

In this section, we propose a model-based policy gradient reinforcement learning (RL) algorithm to train NeuroMHE. This algorithm enables the neural network parameters  $\boldsymbol{\varpi}$  to be learned directly from the trajectory tracking error without the ground-truth disturbance data.

Denote the robust tracking controller by

$$\mathbf{u}_t = \mathbf{u} \left( \mathbf{x}_t^{q,\text{ref}}, \hat{\mathbf{x}}_{t|t} \right), \quad (21)$$

where the estimate  $\hat{\mathbf{x}}_{t|t}$ , consisting of  $\mathbf{x}_t^q$  and  $\mathbf{d}_t$ , is computed online by solving the MHE problem (4). Such a controller can be simply designed as directly compensating the disturbance estimate  $\hat{\mathbf{d}}_{t|t}$  in a nominal geometric flight controller [39]. Supervised learning to train NeuroMHE uses the estimation error  $\left\| \hat{\mathbf{d}}_{t|t} - \mathbf{d}_t \right\|$  as the target, which requires the ground truth disturbance. However, the ground truth  $\mathbf{d}_t$  is often difficult to obtain in practice. Therefore, it is desired to train the NeuroMHE directly from the trajectory tracking errors. For example, the loss function can be chosen as,

$$L(\hat{\mathbf{x}}) = \alpha \sum_{k=t-N}^t \left\| \hat{\mathbf{x}}_{k|t}^q - \mathbf{x}_k^{q,\text{ref}} \right\|_{\mathbf{W}_e}^2, \quad (22)$$

where  $\alpha$  is a positive coefficient and  $\mathbf{W}_e$  is a positive-definite weighting matrix. It penalizes the difference between the estimated quadrotor states by MHE and the reference states.

In training, we perform gradient descent to update  $\boldsymbol{\varpi}$ . We first obtain the analytical gradients  $\frac{\partial \hat{\mathbf{x}}}{\partial \boldsymbol{\theta}}$  using Algorithm 1, then compute  $\frac{\partial L(\hat{\mathbf{x}})}{\partial \hat{\mathbf{x}}}$  and  $\frac{\partial \boldsymbol{\theta}(\boldsymbol{\varpi})}{\partial \boldsymbol{\varpi}}$  from their analytical expressions, and finally apply the chain rule (8) to obtain the gradient  $\frac{dL(\hat{\mathbf{x}})}{d\boldsymbol{\varpi}}$ . We summarize the procedures of training NeuroMHE using the proposed model-based policy gradient RL in Algorithm 2 where  $L_{\text{mean}}$  is the mean value of the loss (22) over one training episode with the duration  $T_{\text{episode}}$ .

**Algorithm 2:** Model-based Policy Gradient RL

---

**Input:** The quadrotor reference trajectory  $\mathbf{x}^{q,\text{ref}}$  and the learning rate  $\varepsilon$

**Initialization:**  $\boldsymbol{\varpi}_0$

**Loss:**  $L(\hat{\mathbf{x}})$  in (22)

```

1  while  $L_{\text{mean}}$  not converged do
2      for  $t \leftarrow 0$  to  $T_{\text{episode}}$  do
3          Compute adaptive weightings  $\boldsymbol{\theta}_t = \mathbf{f}_{\boldsymbol{\varpi}_t}$ ;
4          Solve for  $\hat{\mathbf{x}}$  from the current MHE system (4);
5          ▷ using any numerical
           optimization solver
6          Compute  $\mathbf{u}_t$  from the control law (21);
7          Apply  $\mathbf{u}_t$  to update the quadrotor state  $\mathbf{x}_t^q$ ;
8          Compute  $\frac{\partial \hat{\mathbf{x}}}{\partial \boldsymbol{\theta}}$  using Algorithm 1 given  $\hat{\mathbf{x}}$  and  $\boldsymbol{\theta}_t$ ;
9          Compute  $\frac{\partial L(\hat{\mathbf{x}})}{\partial \hat{\mathbf{x}}}$  from the loss function  $L(\hat{\mathbf{x}})$ ;
10         Compute  $\frac{\partial \boldsymbol{\theta}(\boldsymbol{\varpi})}{\partial \boldsymbol{\varpi}}$  of the NN  $\boldsymbol{\theta}_t = \mathbf{f}_{\boldsymbol{\varpi}_t}$ ;
11         ▷ using any machine learning
           tool
12         Apply the chain rule (8) to obtain  $\frac{dL(\hat{\mathbf{x}})}{d\boldsymbol{\varpi}}$ ;
13         Update  $\boldsymbol{\varpi}_t$  using gradient-based optimization;
14     end for
15 end while

```

---

## VI. CONSTRAINED NEUROMHE

We extend our method to the case where inequality constraints on the system state and the process noise need to be respected in the MHE. This can improve the flight safety by avoiding unrealistic estimation. Without loss of generality, we consider the following constraints for  $k \in [t - N, t]$ :

$$g_{k,i}(\mathbf{x}_k, \mathbf{w}_k) \leq 0, i = 1, \dots, n. \quad (23)$$

By enforcing (23) as hard constraints in the MHE optimization problem, we have:

$$\min_{\mathbf{x}, \mathbf{w}} J \quad (24a)$$

$$\text{s.t. } \mathbf{x}_{k+1} = \mathbf{f}(\mathbf{x}_k, \mathbf{u}_k, \mathbf{w}_k, \Delta t), \quad (24b)$$

$$g_{k,i}(\mathbf{x}_k, \mathbf{w}_k) \leq 0, i = 1, \dots, n, \quad (24c)$$

where  $J$  is the same as defined in (4). We denote the optimal constrained estimates of (24) by  $\hat{\mathbf{x}}_c$  and  $\hat{\mathbf{w}}_c$ . Similar to (4),  $\hat{\mathbf{x}}_c$  is parameterized as  $\hat{\mathbf{x}}_c(\boldsymbol{\theta})$  by the weighting parameters. This method, however, has several implementation difficulties for computing the gradients  $\frac{\partial \hat{\mathbf{x}}_c}{\partial \boldsymbol{\theta}}$ . When differentiating the KKT conditions of (24) with respect to  $\boldsymbol{\theta}$ , one needs to identify all the active constraints  $g_{k,i}(\mathbf{x}_k, \mathbf{w}_k) = 0$ , which can be numerically inefficient. Moreover, the discontinuous

switch between inactive and active inequality constraints may incur numerical instability in learning. Instead of treating (23) as hard constraints, we use interior-point methods to softly penalize (23) in the cost function of the MHE optimization problem. In particular, using the logarithm barrier functions, we have

$$\min_{\mathbf{x}, \mathbf{w}} J - \delta \sum_{k=t-N}^t \sum_{i=1}^n \ln(-g_{k,i}(\mathbf{x}_k, \mathbf{w}_k)) \quad (25a)$$

$$\text{s.t. } \mathbf{x}_{k+1} = \mathbf{f}(\mathbf{x}_k, \mathbf{u}_k, \mathbf{w}_k, \Delta t), \quad (25b)$$

where  $\delta$  is a positive barrier parameter.

Compared with (24), the optimal estimates  $\hat{\mathbf{x}}$  to the soft-constrained MHE problem (25) is now determined by both  $\boldsymbol{\theta}$  and  $\delta$ , denoted by  $\hat{\mathbf{x}}(\boldsymbol{\theta}, \delta)$ . As  $\delta \rightarrow 0$ , we have  $\hat{\mathbf{x}}(\boldsymbol{\theta}, \delta) \rightarrow \hat{\mathbf{x}}_c(\boldsymbol{\theta})$  which is a well-known property of interior-point methods [40], and then we obtain  $\frac{\partial \hat{\mathbf{x}}(\boldsymbol{\theta}, \delta)}{\partial \boldsymbol{\theta}} \rightarrow \frac{\partial \hat{\mathbf{x}}_c(\boldsymbol{\theta})}{\partial \boldsymbol{\theta}}$ . This shows that by setting  $\delta > 0$  to be sufficiently small, we can utilize  $\frac{\partial \hat{\mathbf{x}}(\boldsymbol{\theta}, \delta)}{\partial \boldsymbol{\theta}}$  to approximate  $\frac{\partial \hat{\mathbf{x}}_c(\boldsymbol{\theta})}{\partial \boldsymbol{\theta}}$  with arbitrary accuracy. This allows for applying Algorithm 1 to calculate  $\frac{\partial \hat{\mathbf{x}}(\boldsymbol{\theta}, \delta)}{\partial \boldsymbol{\theta}}$ . Similarly, by parameterizing  $\boldsymbol{\theta}$  in (25) with the neural network (6), we can train the soft-constrained NeuroMHE (25) using Algorithm 2.

## VII. EXPERIMENTS

In this section, we validate the effectiveness of NeuroMHE in robust flight control through both numerical and physical experiments on quadrotors. In particular, we will show the following features of NeuroMHE. First, it enjoys computationally efficient training and significantly improve the force estimation performance as compared to a state-of-the-art estimator (See VII-A). Second, a stable NeuroMHE with a fast dynamic response can be trained directly from the trajectory tracking error using Algorithm 2 (See VII-B). Third, NeuroMHE shows better estimation and robust control performance than a fixed-weighting MHE when the noise covariances are dynamic (See VII-B). Finally, NeuroMHE effectively robustifies a flight controller against challenging external disturbances on a real quadrotor, including sudden payload change and resisting the downwash effect (See VII-C).

In our experiments, we design the neural network to take the quadrotor state  $\mathbf{x}^q$  as input, which we assume is available through onboard sensors or motion capture systems. Hence, we set the measurement of the augmented system (3) to be  $\mathbf{y} = \mathbf{x}^q + \boldsymbol{\nu}$ . A multi-layer perceptron (MLP) network is adopted, and its architecture is depicted in Fig. 2. The MLP has two hidden layers with rectified linear unit (ReLU)  $\phi(x) = \max(x, 0)$  as the activation function. In general, neural networks with ReLU converge faster in training than those with saturating nonlinear functions such as  $\tanh(\cdot)$  [41] and demonstrate superior function approximation ability. The adopted MLP can be expressed mathematically as

$$\mathbf{f}_{\boldsymbol{\varpi}}(\mathbf{y}_t) = \mathbf{A}_o \phi(\mathbf{A}_2 \phi(\mathbf{A}_1 \mathbf{y}_t + \mathbf{b}_1) + \mathbf{b}_2) + \mathbf{b}_o, \quad (26)$$

where  $\{\mathbf{A}_o, \mathbf{A}_1, \mathbf{A}_2\}$  are the weighting matrices,  $\{\mathbf{b}_o, \mathbf{b}_1, \mathbf{b}_2\}$  are the bias vectors, and they are the neural network parameters  $\boldsymbol{\varpi}$  to be learned.

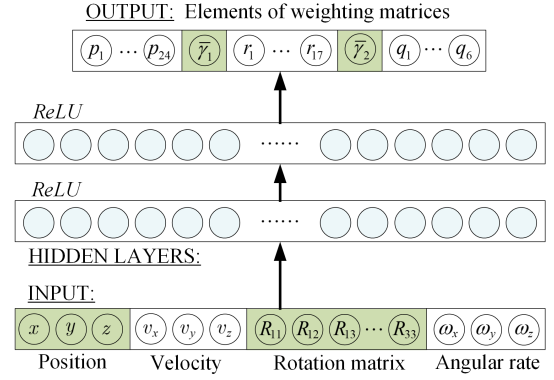


Fig. 2: Architecture of the neural network for generating the adaptive MHE weighting matrices online.

To simplify the modeling of the time-varying weighting matrices  $\mathbf{R}_k$  and  $\mathbf{Q}_k$  in the MHE running cost, we introduce two forgetting factors  $\gamma_{1,2} \in (0, 1)$  and let  $\mathbf{R}_k = \gamma_1^{t-k} \mathbf{R}_t$  for  $k = t - N, \dots, t$  and  $\mathbf{Q}_k = \gamma_2^{t-1-k} \mathbf{Q}_{t-1}$  for  $k = t - N, \dots, t - 1$ . Instead of training a neural network to generate all  $\mathbf{R}_k$  and  $\mathbf{Q}_k$ , we only need to train it to generate adaptive forgetting factors together with adaptive  $\mathbf{P}$ ,  $\mathbf{R}_t$ , and  $\mathbf{Q}_{t-1}$ . This effectively reduces the size of the neural network, keeping it portable while enabling a flexible adjustment of the weights over the horizon. We set  $\mathbf{P} \in \mathbb{R}^{24 \times 24}$ ,  $\mathbf{R}_t \in \mathbb{R}^{18 \times 18}$ , and  $\mathbf{Q}_{t-1} \in \mathbb{R}^{6 \times 6}$  to be diagonal matrices to further reduce the size of the problem. In addition, the first diagonal element in  $\mathbf{R}_t$  is fixed at 100. Then, we train the MLP (26) to tune the remaining 47 diagonal elements and the two forgetting factors, which are collected in the vector  $\boldsymbol{\theta} = [P_{1:24}, \gamma_1, R_{1:17}, \gamma_2, Q_{1:6}]$ . This can improve the training efficiency and optimality, as it reduces the number of local optima for the gradient descent. To ensure  $\mathbf{P}$ ,  $\mathbf{R}_t$ , and  $\mathbf{Q}_{t-1}$  are positive definite, we parameterize the diagonal elements as  $P_{1:24} = \varsigma + p_{1:24}^2$ ,  $R_{1:17} = \varsigma + r_{1:17}^2$ , and  $Q_{1:6} = \varsigma + q_{1:6}^2$ , respectively, where  $\varsigma > 0$  is some pre-chosen small constant. We further use two sigmoid functions to constrain the values of  $\gamma_1$  and  $\gamma_2$  to be in  $(0, 1)$ , and have  $\gamma_{1,2} = (1 + \exp(-\tilde{\gamma}_{1,2}))^{-1}$ . Therefore, the output of the MLP (26) becomes  $\boldsymbol{\Theta} = [p_{1:24}, \tilde{\gamma}_1, r_{1:17}, \tilde{\gamma}_2, q_{1:6}] \in \mathbb{R}^{49}$ , as shown in Fig. 2. The chain rule for the gradient calculation can be written as  $\frac{dL}{d\boldsymbol{\varpi}} = \frac{\partial L}{\partial \mathbf{x}} \frac{\partial \mathbf{x}}{\partial \boldsymbol{\theta}} \frac{\partial \boldsymbol{\theta}}{\partial \boldsymbol{\Theta}} \frac{\partial \boldsymbol{\Theta}}{\partial \boldsymbol{\varpi}}$  to reflect the above parameterization.

We implement our algorithm in Python and use `ipopt` with `CasADi` [37] to solve the nonlinear optimization problem in MHE (4). The MLP (26) is built in PyTorch [42] and is trained<sup>1</sup> using Adam [43].

### A. Efficient Learning for Accurate Estimation

In this numerical experiment, we compare NeuroMHE with the state-of-the-art estimator NeuroBEM [9] to demonstrate the first feature claimed at the beginning of this section. We

<sup>1</sup>In practical implementation, we customize the loss function to suit the typical training procedure in PyTorch. Specifically, we define  $L_{\text{pytorch}} = \frac{\partial L}{\partial \mathbf{x}} \frac{\partial \mathbf{x}}{\partial \boldsymbol{\theta}} \frac{\partial \boldsymbol{\theta}}{\partial \boldsymbol{\Theta}} \boldsymbol{\Theta}$  as the loss function for training the neural network (26) such that  $\frac{dL_{\text{pytorch}}}{d\boldsymbol{\varpi}} = \frac{dL}{d\boldsymbol{\varpi}}$ .

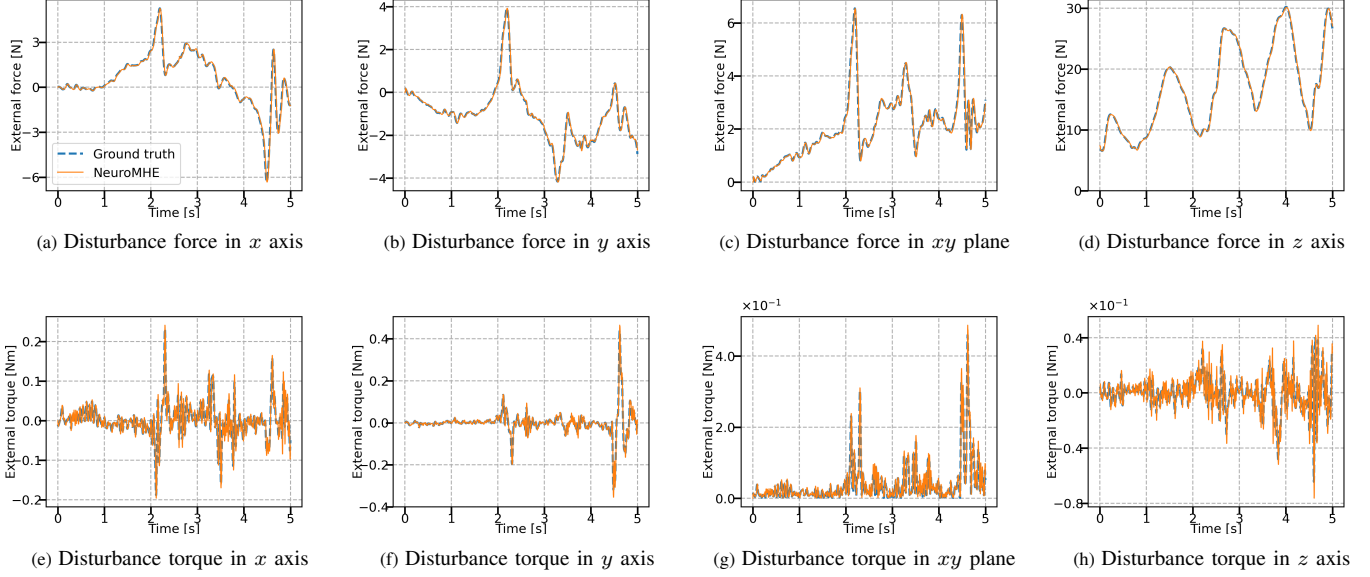


Fig. 3: Evaluation of the force and torque estimation of NeuroMHE on the same test dataset as in [9]. At  $t = 0$ , the initial guess of the disturbance used in the arrival cost is set to be  $\hat{\mathbf{d}}_0 = [0; 0; mg; 0; 0; 0]$  since the quadrotor initially hovers at around 2.15 m. Fig. 3c and 3g are obtained by plotting  $d_{f_{xy}} = \sqrt{d_{f_x}^2 + d_{f_y}^2}$  and  $d_{\tau_{xy}} = \sqrt{d_{\tau_x}^2 + d_{\tau_y}^2}$ , respectively.

use the same flight dataset presented in [9], which is collected in the world's largest indoor motion capture room from various agile and extreme flights. The ground-truth data (quadrotor states and disturbance) can be obtained from the dataset and the model of the experiment quadrotor (1). Hence, we train NeuroMHE from the estimation error using supervised learning. Specifically, we use Algorithm 1 to compute the gradients  $\frac{\partial \mathbf{x}}{\partial \boldsymbol{\theta}}$ , build the loss function  $L$  using the estimation error, and apply gradient descent to update the neural network parameters  $\boldsymbol{\varpi}$ . The ground-truth disturbance forces and torques are computed by

$$\mathbf{d}_f = m\mathbf{R}^T (\mathbf{a}_v + g\mathbf{z}), \quad \mathbf{d}_\tau = \mathbf{J}\mathbf{a}_\omega + \boldsymbol{\omega}^\times \mathbf{J}\boldsymbol{\omega}, \quad (27)$$

where  $\mathbf{J} = \text{diag}(2.52, 2.14, 4.36) \times 10^{-3} \text{ kg m}^2$  and  $m = 0.752 \text{ kg}$  as used in [9],  $\mathbf{a}_v$  and  $\mathbf{a}_\omega$  are the linear and angular accelerations given in the dataset. Note that for the convenience of comparison, here  $\mathbf{d}_f$  (which is expressed in the body frame for the convenience of comparison) and  $\mathbf{d}_\tau$  include respectively the total thrust and the control torques generated by the quadrotor motors as did in [9]. For NeuroMHE, the dynamics model (1) is discretized using forward Euler method using the same time step of 2.5 ms as in the dataset. Each hidden layer of the neural network has 100 neurons. For the training data, we choose a representative segment of 2.5 s long from a figure-8 flight, which covers a wide range of velocity from  $1 \text{ m s}^{-1}$  to  $15.15 \text{ m s}^{-1}$  and multiple force spikes. One training episode amounts to train the NeuroMHE over this 2.5 s long data once. For the test data, we use the same dataset as in [9] to compare NeuroMHE with NeuroBEM on another figure-8 trajectory (which is unseen in our training dataset).

Table I summarizes the runtime of Algorithm 1 for different MHE horizons. The runtime is approximately linear to the horizon, thus the algorithm can scale efficiently to a large MHE problem with a long horizon. This is made possible

TABLE I  
RUNTIME OF ALGORITHM 1 UNDER DIFFERENT HORIZONS

Horizon $N$	10	20	40	60	80	100
Runtime [ms]	3.45	6.27	12.02	17.6	23.87	29.55

The time is measured in a workstation with the processor of 11th Gen Intel Core i7 – 11700K.

because of the proposed Kalman filter based gradient solver (Algorithm 1), which has a linear computational complexity with respect to the number of horizons  $N$ . Given the quadrotor's fast dynamics in extreme flights, we set  $N = 10$  in the training.

In Fig. 3, we plot the NeuroMHE estimation and the ground truth disturbances of the test dataset. The force estimates can converge quickly to the ground truth data from the initial guess within about 0.1 s. The estimation is of high accuracy even around the most fast changing spikes of  $d_{f_x}$  and  $d_{f_y}$  (see Fig. 3a and 3b). The torque estimates also show satisfactory performance but are slightly noisier than the force estimates. To compare with NeuroBEM, we quantify the estimation performance using the Root-Mean-Square error (RMSEs) and summarize the comparison in Table II. Overall, NeuroMHE thrust estimation error is 25% smaller than that of NeuroBEM (see the 5th data column). It substantially outperforms NeuroBEM in the planar and the vertical forces estimation with estimation error reductions of 41.2% and 49.4%, respectively. We further test the same trained NeuroMHE on other flight dataset of different trajectories, such as random flights and racing flights. NeuroMHE shows similar accurate estimation performances over all the tested data (e.g., the RMSEs of  $d_f$  are 0.262 N and 0.108 N for a random trajectory and a racing trajectory, respectively).

As a consequence of combining a portable neural network

TABLE II  
ESTIMATION ERRORS (RMSEs) COMPARISONS

Method	$d_{f_{xy}}$ [N]	$d_{f_z}$ [N]	$d_{\tau_{xy}}$ [Nm]	$d_{\tau_z}$ [Nm]	$d_f$ [N]	$d_\tau$ [Nm]
NeuroBEM	0.204	0.504	0.014	<b>0.004</b>	0.335	<b>0.012</b>
NeuroMHE	<b>0.120</b>	<b>0.255</b>	<b>0.013</b>	0.006	<b>0.251</b>	0.013

The RMSEs of NeuroBEM are transcribed from [9]. The torque estimate of NeuroMHE in the  $z$  direction is slightly worse than that of NeuroBEM. This is mainly because  $d_{\tau_z}$  is much smaller than the others, making it hard to estimate.

with the model-based MHE estimator, our auto-tuning/training algorithm is very data-efficient. For example, NeuroBEM requires 1.26 million data points for training a much more complicated neural network consisting of temporal-convolutional layers and MLP layers with 25k parameters. In contrast, our method uses only 1k data points to train less than 2.5% neural network parameters (about 0.5k) and achieve up to 49.4% better performance in the force estimation.

### B. Online Learning with Fast Adaptation

Furthermore, we design a robust trajectory tracking control scenario in simulation to show the second and third features of our algorithm. We synthesize the external disturbances by integrating the random walk model (2), where  $w_f \sim \mathcal{N}(0, \sigma_f)$  and  $w_\tau \sim \mathcal{N}(0, \sigma_\tau)$  are set to be Gaussian noises with standard deviations modeled by two polynomials of the quadrotor state, i.e.,  $\sigma_f = c_v \text{diag}^2(v) + c_p \text{diag}^2(p) + c_f$  and  $\sigma_\tau = c_\omega \text{diag}^2(\omega) + c_\Theta \text{diag}^2(\Theta_e) + c_\tau$  where  $\Theta_e$  denotes the Euler angles of the quadrotor,  $c_v$ ,  $c_p$ ,  $c_f$ ,  $c_\omega$ ,  $c_\Theta$ , and  $c_\tau$  are  $3 \times 3$  diagonal positive definite coefficient matrices. Given the fact that the underactuation of quadrotors makes the horizontal forces much harder to compensate for than the vertical disturbance [44], we set the 3rd elements in  $c_v$  and  $c_p$  to be 3 times larger than the others, leading to the major disturbance force in the  $z$  direction (see the arrows in Fig. 4). The coefficients in  $\sigma_\tau$  are set to be at the order of  $10^{-2}$ , which is consistent with the relative small aerodynamic torques in common flights. We generate a disturbance dataset offline for training by setting  $v$ ,  $p$ ,  $\Theta_e$ , and  $\omega$  in  $\sigma_f$  and  $\sigma_\tau$  to be the desired quadrotor states on the reference trajectory.

To highlight the benefits of the adaptive weightings, we compare NeuroMHE against a fixed-weighting MHE. The latter is automatically tuned using gradient descent on the same disturbance dataset and is referred to as differentiable moving horizon estimator (DMHE). Specifically, to train DMHE, we first use Algorithm 1 to compute the gradients  $\frac{\partial \hat{x}}{\partial \theta}$ , then obtain the gradient of the loss function with respect to  $\theta$  using the chain rule  $\frac{dL(\hat{x}(\theta))}{d\theta} = \frac{\partial L(\hat{x})}{\partial \hat{x}} \frac{\partial \hat{x}(\theta)}{\partial \theta}$ , and finally apply gradient descent to update  $\theta$ . Different from the adaptive weightings of NeuroMHE, the weightings of DMHE are fixed at their optimal values  $\theta^*$ .

We develop the robust flight controller (21) based on the geometric controller proposed in [39]. Before training, the parameters of the geometric controller are manually tuned until the best performance is achieved in an ideal case where no external disturbances act on the quadrotor. Then, we include the current disturbance estimate from NeuroMHE as

a feedforward term in the controller to compensate for the disturbance. Given the current  $x_t^q$ ,  $u_t$ , and  $d_t$ , the quadrotor model (1) is integrated using 4th-order Runge-kutta method with a fixed time step of 10 ms to update  $y_t$ . We set the measurement noise  $v$  to be Gaussian and its fixed covariance matrix to be much smaller than those of  $w_f$  and  $w_\tau$ . The same numerical integration is used in NeuroMHE for the state prediction. Finally, the number of neurons in both hidden layers is 50, and the MHE horizon is 10.

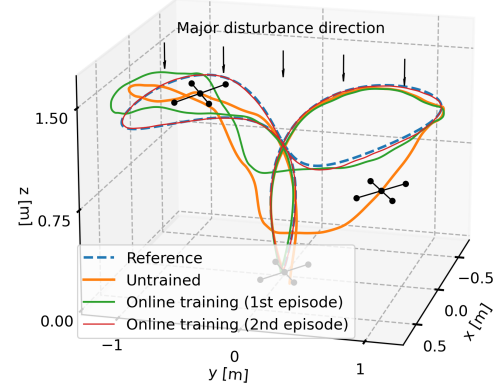
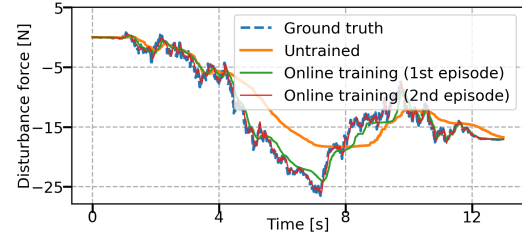
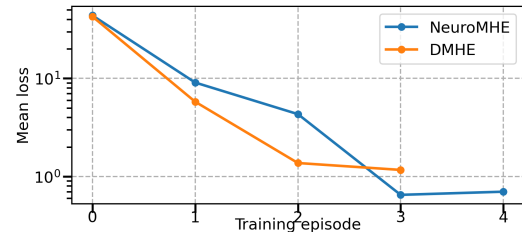


Fig. 4: Trajectory tracking performance of NeuroMHE in training. The quadrotor is controlled to take off, follow a figure-8 trajectory, and finally land at the starting point. The video demos can be found at <https://youtu.be/Z68zwvhL0XE>.



(a) Disturbance force in  $z$  direction in training



(b) Mean loss in training

Fig. 5: Force estimates of NeuroMHE in training and comparison of the mean loss. For the sake of comparison, the initial  $\theta_0$  of DMHE is manually tuned such that the untrained mean loss is very close to that of NeuroMHE.

We begin with visualizing the training process by a 3D trajectory plot in Fig. 4. It shows that the height tracking performance is substantially improved online. Remarkably, the quadrotor can already track the reference trajectory accurately starting merely from the 2nd training episode. The force estimation in the  $z$  direction (see Fig. 5a) was compared in different training episodes. We further observe in Fig. 5b that although the mean loss of NeuroMHE converges slightly

slower than that of DMHE (due to more parameters to train), its steady value is much smaller, indicating better tracking performance.

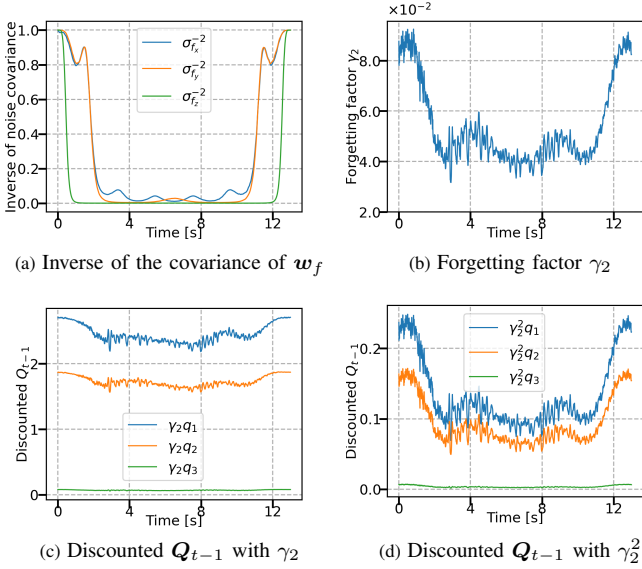


Fig. 6: Comparison of the inverse of the noise covariance parameters and the NeuroMHE weighting matrices on the unseen synthetic disturbance dataset. Here, we show two examples of the discounted  $\gamma_2 \mathbf{Q}_{t-1}$  and  $\gamma_2^2 \mathbf{Q}_{t-1}$ , respectively. The remaining  $\mathbf{Q}_k = \gamma_2^{t-1-k} \mathbf{Q}_{t-1}$  with  $k = t - N, \dots, t - 4$  have the similar changing pattern.

To evaluate the trained robust controller, we generate another disturbance dataset offline by integrating the random walk model (2) with the same noise covariance parameters as in training. In Fig. 6, we plot the inverse of the covariance parameters of  $\mathbf{w}_f$  and the weighting matrices that penalize  $\mathbf{w}_f$  in the MHE cost function (4a). The forgetting factor  $\gamma_2$  and the discounted elements of  $\mathbf{Q}_{t-1}$  change with time in a similar way to the inverse of the covariance parameters of  $\mathbf{w}_f$ . This same changing pattern indicates that the neural network enables the weightings to adapt to the quadrotor state correctly. The forgetting factor  $\gamma_1$  is much larger than  $\gamma_2$  and settles around 0.98, which is consistent with the very small and fixed measurement noise covariance. For DMHE, the optimized  $\gamma_1^*$  and  $\gamma_2^*$  are 0.746 and 0.209, and the optimized  $q_1^*_{\sim 3}$  are 0.991, 0.98, and 0.566, respectively.

We compare these two methods' force estimation and trajectory tracking performances in Fig. 7. With the neural network, the time-varying  $\gamma_2$  decreases to allow for rapid changes of the force estimates in the period of 3 ~ 10 s, thus enabling NeuroMHE to track the fast-changing disturbance forces during that period accurately. In contrast, without the neural network, the force estimates of DMHE have more significant estimation error and lag than those of NeuroMHE (see the zoom-in window of Fig. 7c), leading to a larger height tracking error shown in Fig. 7d.

The above results suggest that a small  $\mathbf{Q}_k$  is more likely to perform well for the disturbance estimation. To validate this, we manually tune  $\mathbf{Q}_k$  to be extremely small by setting  $\gamma_2$  and the diagonal elements of  $\mathbf{Q}_{t-1}$  to be 0.01 and  $1 \times 10^{-4}$ , respectively. As shown in Fig. 7a, 7b, and 7c, although the force estimation performance of this manually-tuned MHE

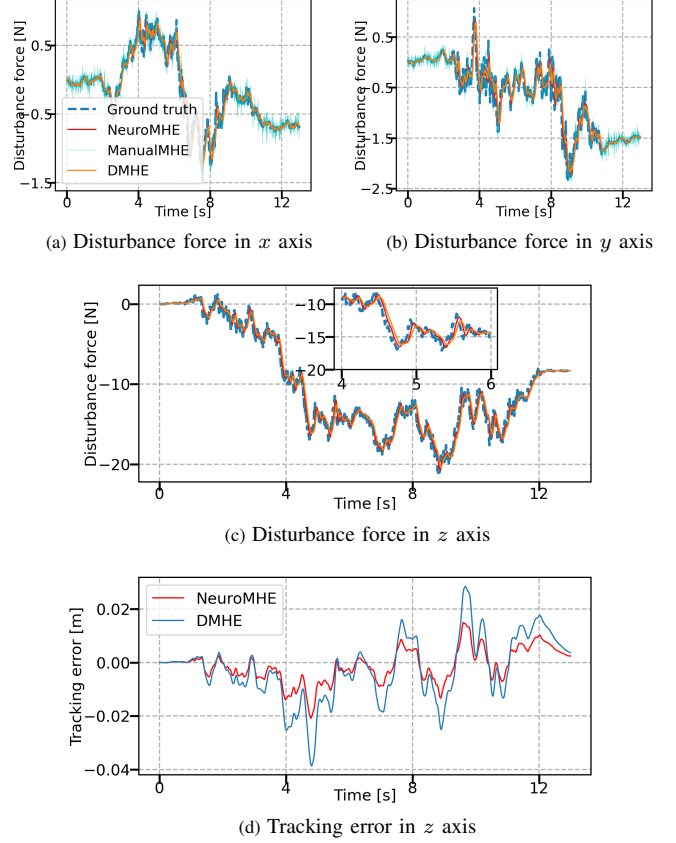


Fig. 7: Comparison of the force estimates and tracking errors in evaluation on the unseen synthetic disturbance dataset.

is comparable to NeuroMHE in the period of 3 ~ 10 s, its performance degrades substantially, and the force estimates are very oscillatory when the disturbance forces become slowly-varying outside that period. Such high-frequency oscillations will lead to severe stability issues for the control system. On the contrary, a well-trained NeuroMHE is more stable during the whole episode.

We further compare NeuroMHE with DMHE over 100 episodes. In each episode, the quadrotor is controlled to track the same reference trajectory as in training, and the external disturbances are updated online by integrating the random walk model with the state-dependent noise based on the current quadrotor state. In Fig. 8, we present boxplots of the RMSEs in terms of the force estimation error and the trajectory tracking error. Fig. 8a shows that the estimation performance of NeuroMHE for the horizontal disturbance forces are slightly better than that of DMHE, but a significant improvement is in the  $z$  direction with a 20% RMSE reduction<sup>2</sup>. Accordingly, Fig. 8b shows that NeuroMHE outperforms DMHE significantly in the  $z$  direction with 42% better height tracking performance.

Overall, our simulation results indicate:

<sup>2</sup>Based on the boxplots in Fig. 8, we further quantify the performance using the medians of the RMSEs. Specifically, we compute the performance index by  $p_{\text{rate}} = \frac{m_{\text{DMHE}} - m_{\text{NeuroMHE}}}{m_{\text{DMHE}}} \times 100\%$  where  $m_{\text{DMHE}}$  and  $m_{\text{NeuroMHE}}$  denote the medians of the RMSEs of DMHE and NeuroMHE, respectively. A positive  $p_{\text{rate}}$  represents that NeuroMHE outperforms DMHE.

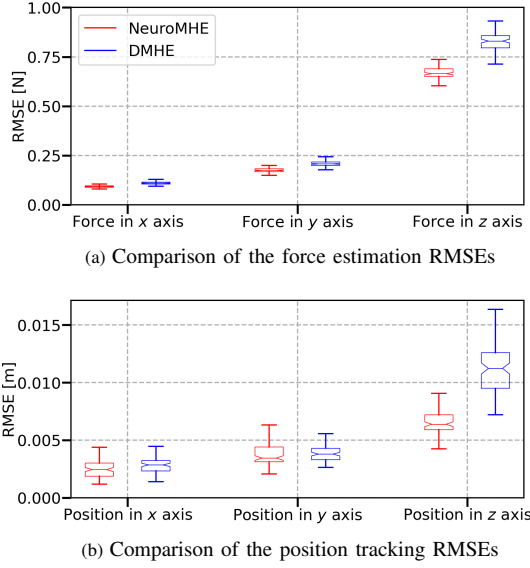


Fig. 8: Boxplots of testing the estimation and trajectory tracking performance in terms of the RMSEs over 100 episodes. The 25th and 75th percentiles of each box are marked by the bottom and top edges. The line in each box denotes the median value. All the outliers are removed. Compared with the results in Table II, the RMSEs of NeuroMHE are larger as the disturbance forces are more noisy than those in the real dataset.

- 1) A stable NeuroMHE with a fast dynamic response can be efficiently learned online in merely a few episodes from the quadrotor trajectory tracking error without the need for the ground-truth disturbance data.
- 2) The neural network can generate the adaptive weightings online, thus improving both the estimation and control performance of the NeuroMHE-augmented flight controller when the noise covariances are dynamic.

### C. Physical Experiments

Finally, we validate the robust flight control performance of using NeuroMHE on a real quadrotor against various external disturbances. The baseline controller consists of a NN-parameterized Proportional-Derivative (NN-PD) controller with a gravity compensation. In the robust version of the controller, additionally, the estimated disturbance by NeuroMHE is included as a feedforward term to compensate the disturbance. We evaluate the robust controller in two experiments: 1) stabilization under sudden payload change, and 2) stabilization and holding the position against downwash. The setup of the hardware platform is outlined in Figure 9. The training of NeuralMHE is performed in numerical simulation, where the quadrotor is commanded to take off with the tethered load and release it repeatedly. Such an effect is simulated numerically using a square-wave signal, and its magnitude is randomly set at the beginning of each training episode. Since the force estimation and position dynamics are the primary concern in the experiment, we modify the output of the neural network to be  $\Theta = [p_{1:9}, \tilde{\gamma}_1, r_{1:6}, \tilde{\gamma}_2, q_{1:3}] \in \mathbb{R}^{20}$ , excluding the weightings related to the quadrotor attitude and angular velocities. The number of neurons is 50 in both hidden layers. Finally, the trained NeuroMHE and NN-PD

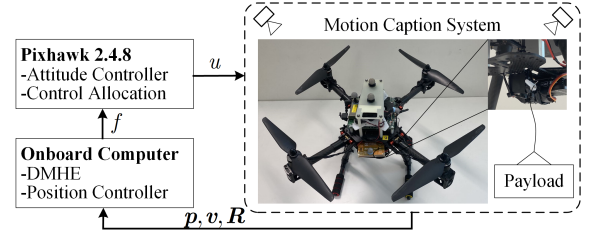


Fig. 9: Overview of the hardware components where the quadrotor weighs 1.8 kg and the on-board computer running ROS melodic is the 64-bit *Intel nuc* with the processor of *Intel Core i7-5557U CPU*.

controller are deployed directly to the real quadrotor without extra tuning.

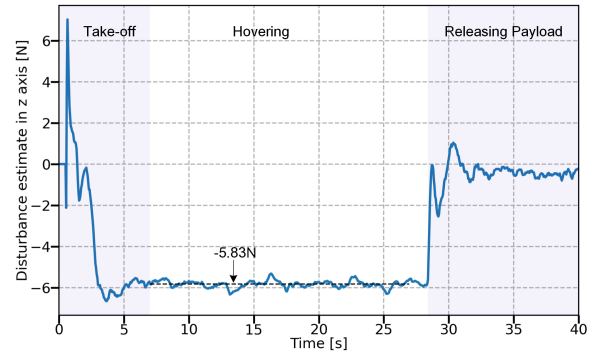


Fig. 10: Estimate of disturbance force in  $z$ -direction posed by the payload in the *East-North-Up* inertial frame. The average of the estimated force is  $-5.83$  N which is accurate compared to the ground truth of  $-5.87$  N. The payload is released at around 28 s and NeuroMHE can respond to this sudden change quickly. The initial estimated force mainly comes from the ground effect which provides the quadrotor with extra lift.

Before the fly tests, we first use a payload of known weight (600 g) to calibrate NeuroMHE in order to remove the systematic constant bias presented in the estimation. The first experiment is to test the dynamic response of NeuroMHE to a step-disturbance. To this end, the quadrotor is controlled to take off with the payload and release it once hovering at the 1.5 m height setpoint. The payload is tethered to the quadrotor using a cable of length 0.4 m. At around 28 s in Fig. 10, the payload is released, and NeuroMHE responds to this sudden change quickly with a rising time less than 0.5 s. The external force posed by the payload (during about 7 ~ 28 s in Fig. 10) is estimated by NeuroMHE to be  $-5.83$  N with a standard deviation of 0.03 N. This is a satisfactory estimation compared with the true weight of  $0.6 \text{ kg} \times 9.78 \text{ m s}^{-2} \approx 5.87$  N using the local gravitational acceleration in Singapore.

The second experiment tests the robustness of the proposed method against the downwash effect. Passing through the downwash airflow generated by another quadrotor can cause a significant loss of lift (see Fig. 12) and thus leads to catastrophic failure. We first program the ego quadrotor (see the setup in Fig. 9) to automatically take off and hover at 1.5 m. Then, a second quadrotor is controlled to hover at about 2.2 m and right above the ego one (see Fig. 11, which begins at around 30 s in Fig. 13). We can see from Fig. 13 that the NeuroMHE compensation enables the ego quadrotor

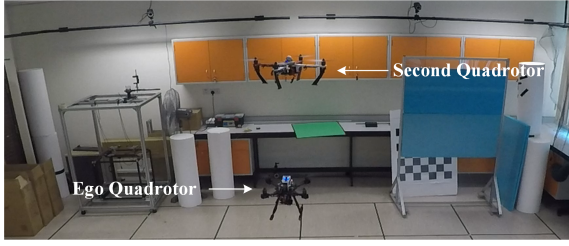


Fig. 11: Illustration of the downwash experiment. The second quadrotor hovers at about 0.7 m above the ego one, which begins at 30 s to produce the downwash effect. The width of the second quadrotor is 0.3 m.

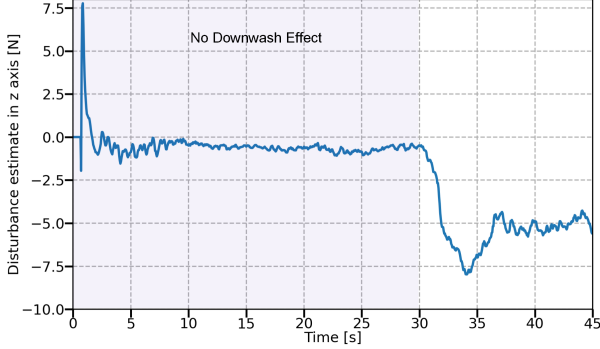


Fig. 12: Estimation of aerodynamic disturbance force caused by the downwash effect. Same as Fig. 10, the initial ( $< 2$  s) estimated force spike mainly comes from the ground effect which provides the quadrotor with extra lift. The small steady disturbance of about 0.7 N during  $17 \sim 30$  s is caused by the aerodynamic interaction between the two quadrotors.

to maintain at the desired height after a mild oscillation with a small amplitude. In contrast, with the baseline controller alone, there is a severe oscillation starting 30 s. The ego quadrotor cannot hold the desired height, and is pushed down to about 1 m high above the ground.

The above experiments using real quadrotors demonstrates that NeuroMHE can effectively robustify a baseline flight controller against strong external disturbances.

## VIII. CONCLUSION

This paper proposed a novel estimator NeuroMHE that can accurately estimate the external disturbances and adapt to different flight scenarios. Our critical insight is that NeuroMHE can automatically tune the key parameters generated by a neural network online from the trajectory tracking error to achieve optimal performance. At the core of our approach is the computationally efficient method to obtain the analytical gradients of the MHE estimates with respect to the weightings, which explores a recursive form using a Kalman filter. We have shown that the proposed NeuroMHE enjoys efficient training, fast online environment adaptation, and improved force estimation performance over the state-of-the-art estimator, via extensive simulations using both real and synthetic datasets. We have also conducted physical experiments on a real quadrotor to demonstrate that NeuroMHE can effectively robustify a baseline flight controller against various challenging external disturbances. Our future work includes developing more efficient training algorithms, simultaneous

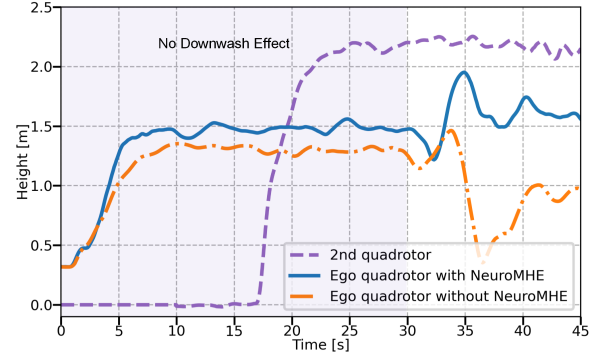


Fig. 13: Comparison of hovering under the downwash effect between the NN-PD baseline controller and the proposed controller. The ego quadrotor is programmed to take off without the payload and hover at 1.5 m height setpoint. After that, we make the second quadrotor fly and hover at 0.7 m above the ego one, which begins at around 30 s. Because only the disturbance forces are compensated, the proposed controller takes time to suppress the oscillation due to the coupling with the perturbed rotational dynamics.

learning of estimator and controller, and analyzing the stability of NeuroMHE.

## ACKNOWLEDGEMENT

We thank Leonard Bauersfeld for the help on using the flight dataset of NeuroBEM.

## REFERENCES

- [1] W. Hönig, J. A. Preiss, T. S. Kumar, G. S. Sukhatme, and N. Ayanian, "Trajectory planning for quadrotor swarms," *IEEE Transactions on Robotics*, vol. 34, no. 4, pp. 856–869, 2018.
- [2] S. Gupte, P. I. T. Mohandas, and J. M. Conrad, "A survey of quadrotor unmanned aerial vehicles," in *2012 Proceedings of IEEE Southeastcon*. IEEE, 2012, pp. 1–6.
- [3] M. Brunner, L. Giacomini, R. Siegwart, and M. Tognon, "Energy tank-based policies for robust aerial physical interaction with moving objects," *arXiv preprint arXiv:2202.06755*, 2022.
- [4] J. Geng and J. W. Langelaan, "Cooperative transport of a slung load using load-leading control," *Journal of Guidance, Control, and Dynamics*, vol. 43, no. 7, pp. 1313–1331, 2020.
- [5] B. E. Jackson, T. A. Howell, K. Shah, M. Schwager, and Z. Manchester, "Scalable cooperative transport of cable-suspended loads with uavs using distributed trajectory optimization," *IEEE Robotics and Automation Letters*, vol. 5, no. 2, pp. 3368–3374, 2020.
- [6] N. Michael, D. Mellinger, Q. Lindsey, and V. Kumar, "The grasp multiple micro-uav testbed," *IEEE Robotics & Automation Magazine*, vol. 17, no. 3, pp. 56–65, 2010.
- [7] C. Powers, D. Mellinger, A. Kushleyev, B. Kothmann, and V. Kumar, "Influence of aerodynamics and proximity effects in quadrotor flight," in *Experimental robotics*. Springer, 2013, pp. 289–302.
- [8] Y. Naka and A. Kagami, "Coanda effect of a propeller airflow and its aerodynamic impact on the thrust," *Journal of Fluid Science and Technology*, vol. 15, no. 3, pp. JFST0016–JFST0016, 2020.
- [9] L. Bauersfeld, E. Kaufmann, P. Foehn, S. Sun, and D. Scaramuzza, "Neurobem: Hybrid aerodynamic quadrotor model," *arXiv preprint arXiv:2106.08015*, 2021.
- [10] G. Shi, W. Hönig, X. Shi, Y. Yue, and S.-J. Chung, "Neural-swarm2: Planning and control of heterogeneous multirotor swarms using learned interactions," *IEEE Transactions on Robotics*, 2021.
- [11] S. Belkhal, R. Li, G. Kahn, R. McAllister, R. Calandra, and S. Levine, "Model-based meta-reinforcement learning for flight with suspended payloads," *IEEE Robotics and Automation Letters*, vol. 6, no. 2, pp. 1471–1478, 2021.
- [12] F. Ruggiero, J. Cacace, H. Sadeghian, and V. Lippiello, "Impedance control of VTOL uavs with a momentum-based external generalized forces estimator," in *2014 IEEE International Conference on Robotics and Automation (ICRA)*, 2014, pp. 2093–2099.

- [13] B. Yüksel, C. Secchi, H. H. Bühlhoff, and A. Franchi, “A nonlinear force observer for quadrotors and application to physical interactive tasks,” in *2014 IEEE/ASME international conference on advanced intelligent mechatronics*. IEEE, 2014, pp. 433–440.
- [14] T. Tomić and S. Haddadin, “A unified framework for external wrench estimation, interaction control and collision reflexes for flying robots,” in *2014 IEEE/RSJ International Conference on Intelligent Robots and Systems*. IEEE, 2014, pp. 4197–4204.
- [15] K. Bodie, M. Brunner, M. Pantic, S. Walser, P. Pfändler, U. Angst, R. Siegwart, and J. Nieto, “Active interaction force control for contact-based inspection with a fully actuated aerial vehicle,” *IEEE Transactions on Robotics*, vol. 37, no. 3, pp. 709–722, 2021.
- [16] C. D. McKinnon and A. P. Schoellig, “Estimating and reacting to forces and torques resulting from common aerodynamic disturbances acting on quadrotors,” *Robotics and Autonomous Systems*, vol. 123, p. 103314, 2020.
- [17] A. Punjani and P. Abbeel, “Deep learning helicopter dynamics models,” in *2015 IEEE International Conference on Robotics and Automation (ICRA)*. IEEE, 2015, pp. 3223–3230.
- [18] N. Mohajerin, M. Mozifian, and S. Waslander, “Deep learning a quadrotor dynamic model for multi-step prediction,” in *2018 IEEE International Conference on Robotics and Automation (ICRA)*. IEEE, 2018, pp. 2454–2459.
- [19] M. Diehl, H. J. Ferreau, and N. Haverbeke, “Efficient numerical methods for nonlinear MPC and moving horizon estimation,” in *Nonlinear model predictive control*. Springer, 2009, pp. 391–417.
- [20] S. S. Mansouri, H. Jafari, and G. Nikolakopoulos, “External force estimation based on nonlinear moving horizon estimation for mav navigation,” in *2020 European Control Conference (ECC)*, 2020, pp. 1312–1317.
- [21] A. Wenz and T. A. Johansen, “Moving horizon estimation of air data parameters for uavs,” *IEEE Transactions on Aerospace and Electronic Systems*, vol. 56, no. 3, pp. 2101–2121, 2019.
- [22] M. Osman, M. W. Mehrez, M. A. Daoud, A. Hussein, S. Jeon, and W. Melek, “A generic multi-sensor fusion scheme for localization of autonomous platforms using moving horizon estimation,” *Transactions of the Institute of Measurement and Control*, vol. 43, no. 15, pp. 3413–3427, 2021.
- [23] A. Eltrabyly, D. Ichalal, and S. Mammar, “Quadcopter trajectory tracking in the presence of 4 faulty actuators: A nonlinear MHE and MPC approach,” *IEEE Control Systems Letters*, vol. 6, pp. 2024–2029, 2021.
- [24] Y. Hu, C. Gao, and W. Jing, “Joint state and parameter estimation for hypersonic glide vehicles based on moving horizon estimation via carleman linearization,” *Aerospace*, vol. 9, no. 4, p. 217, 2022.
- [25] D. G. Robertson, J. H. Lee, and J. B. Rawlings, “A moving horizon-based approach for least-squares estimation,” *AIChE Journal*, vol. 42, no. 8, pp. 2209–2224, 1996.
- [26] A. Y. Aravkin and J. V. Burke, “Smoothing dynamic systems with state-dependent covariance matrices,” in *53rd IEEE Conference on Decision and Control*. IEEE, 2014, pp. 3382–3387.
- [27] C. Nguyen Van, “State estimation based on sigma point kalman filter for suspension system in presence of road excitation influenced by velocity of the car,” *Journal of Control Science and Engineering*, vol. 2019, 2019.
- [28] B. Amos and J. Z. Kolter, “OptNet: Differentiable optimization as a layer in neural networks,” in *International Conference on Machine Learning*. PMLR, 2017, pp. 136–145.
- [29] B. Amos, I. D. J. Rodriguez, J. Sacks, B. Boots, and J. Z. Kolter, “Differentiable MPC for end-to-end planning and control,” in *Proceedings of the 32nd International Conference on Neural Information Processing Systems*, 2018, pp. 8299–8310.
- [30] W. Jin, Z. Wang, Z. Yang, and S. Mou, “Pontryagin differentiable programming: An end-to-end learning and control framework,” *Advances in Neural Information Processing Systems*, vol. 33, 2020.
- [31] W. Jin, S. Mou, and G. J. Pappas, “Safe pontryagin differentiable programming,” *Advances in Neural Information Processing Systems*, vol. 34, pp. 16034–16050, 2021.
- [32] H. N. Esfahani, A. B. Kordabad, and S. Gros, “Reinforcement learning based on MPC/MHE for unmodeled and partially observable dynamics,” in *2021 American Control Conference (ACC)*, 2021, pp. 2121–2126.
- [33] S. Muntwiler, K. P. Wabersich, and M. N. Zeilinger, “Learning-based moving horizon estimation through differentiable convex optimization layers,” *arXiv preprint arXiv:2109.03962*, 2021.
- [34] B. Wang, Z. Ma, S. Lai, L. Zhao, and T. H. Lee, “Differentiable moving horizon estimation for robust flight control,” in *2021 60th IEEE Conference on Decision and Control (CDC)*. IEEE, 2021, pp. 3563–3568.
- [35] A. Alessandri, M. Baglietto, G. Battistelli, and V. Zavala, “Advances in moving horizon estimation for nonlinear systems,” in *49th IEEE Conference on Decision and Control (CDC)*. IEEE, 2010, pp. 5681–5688.
- [36] C. V. Rao, J. B. Rawlings, and D. Q. Mayne, “Constrained state estimation for nonlinear discrete-time systems: Stability and moving horizon approximations,” *IEEE transactions on automatic control*, vol. 48, no. 2, pp. 246–258, 2003.
- [37] J. A. Andersson, J. Gillis, G. Horn, J. B. Rawlings, and M. Diehl, “Casadi: a software framework for nonlinear optimization and optimal control,” *Mathematical Programming Computation*, vol. 11, no. 1, pp. 1–36, 2019.
- [38] H. Cox, “Estimation of state variables for noisy dynamic systems,” Ph.D. dissertation, Massachusetts Institute of Technology, 1963.
- [39] T. Lee, M. Leok, and N. H. McClamroch, “Geometric tracking control of a quadrotor UAV on SE(3),” in *49th IEEE conference on decision and control (CDC)*. IEEE, 2010, pp. 5420–5425.
- [40] A. Forsgren, P. E. Gill, and M. H. Wright, “Interior methods for nonlinear optimization,” *SIAM review*, vol. 44, no. 4, pp. 525–597, 2002.
- [41] A. Krizhevsky, I. Sutskever, and G. E. Hinton, “Imagenet classification with deep convolutional neural networks,” *Advances in neural information processing systems*, vol. 25, pp. 1097–1105, 2012.
- [42] A. Paszke, S. Gross, F. Massa, A. Lerer, J. Bradbury, G. Chanan, T. Killeen, Z. Lin, N. Gimelshein, L. Antiga *et al.*, “Pytorch: An imperative style, high-performance deep learning library,” *Advances in neural information processing systems*, vol. 32, pp. 8026–8037, 2019.
- [43] D. P. Kingma and J. Ba, “Adam: A method for stochastic optimization,” *arXiv preprint arXiv:1412.6980*, 2014.
- [44] D. Hanover, P. Foehn, S. Sun, E. Kaufmann, and D. Scaramuzza, “Performance, precision, and payloads: Adaptive nonlinear MPC for quadrotors,” *IEEE Robotics and Automation Letters*, vol. 7, no. 2, pp. 690–697, 2021.

## APPENDIX

### A. Proof of Lemma 1

For the auxiliary MHE system (16), we define the following Lagrangian

$$\mathcal{L}_2 = \frac{1}{2} \text{Tr} \left\| \mathbf{X}_{t-N} - \hat{\mathbf{X}}_{t-N} \right\|_{\mathbf{P}}^2 + \bar{\mathcal{L}}_2, \quad (28)$$

where

$$\begin{aligned} \bar{\mathcal{L}}_2 = & \text{Tr} \sum_{k=t-N}^t \left( \frac{1}{2} \mathbf{X}_k^T \bar{\mathbf{L}}_k^{xx} \mathbf{X}_k + \mathbf{W}_k^T \mathbf{L}_k^{wx} \mathbf{X}_k \right) \\ & + \text{Tr} \sum_{k=t-N}^{t-1} \left( \frac{1}{2} \mathbf{W}_k^T \mathbf{L}_k^{ww} \mathbf{W}_k + (\mathbf{L}_k^{w\theta})^T \mathbf{W}_k \right) \\ & + \text{Tr} \sum_{k=t-N}^t \left( (\mathbf{L}_k^{x\theta})^T \mathbf{X}_k \right) \\ & + \text{Tr} \sum_{k=t-N}^{t-1} \mathbf{\Lambda}_k^T (\mathbf{X}_{k+1} - \mathbf{F}_k \mathbf{X}_k - \mathbf{G}_k \mathbf{W}_k). \end{aligned}$$

The optimal estimates  $\hat{\mathbf{X}}$  and  $\hat{\mathbf{W}}$ , together with the new optimal dual variables  $\mathbf{\Lambda}^* = \{\mathbf{\Lambda}_k^*\}_{k=t-N}^{t-1}$ , satisfy the following

KKT conditions:

$$\begin{aligned} \nabla_{X_{t-N}} \mathcal{L}_2 = & (P + \bar{L}_{t-N}^{xx}) \hat{X}_{t-N|t} - P \hat{X}_{t-N} + L_{t-N}^{x\theta} \\ & + L_{t-N}^{xw} \hat{W}_{t-N|t} - F_{t-N}^T \Lambda_{t-N}^* = 0, \end{aligned} \quad (29a)$$

$$\begin{aligned} \nabla_{X_k} \mathcal{L}_2 = & \bar{L}_k^{xx} \hat{X}_{k|t} + L_k^{xw} \hat{W}_{k|t} - F_k^T \Lambda_k^* + \Lambda_{k-1}^* \\ & + L_k^{x\theta} = 0, \quad k = t - N + 1, \dots, t, \end{aligned} \quad (29b)$$

$$\begin{aligned} \nabla_{W_k} \mathcal{L}_2 = & L_k^{wx} \hat{X}_{k|t} + L_k^{ww} \hat{W}_{k|t} - G_k^T \Lambda_k^* \\ & + L_k^{w\theta} = 0, \quad k = t - N, \dots, t - 1, \end{aligned} \quad (29c)$$

$$\begin{aligned} \nabla_{\Lambda_k} \mathcal{L}_2 = & \hat{X}_{k+1|t} - F_k \hat{X}_{k|t} - G_k \hat{W}_{k|t} = 0, \\ & k = t - N, \dots, t - 1. \end{aligned} \quad (29d)$$

The above equations (29) are the same as the differential KKT conditions (13), and thus (15) holds. This completes the proof.

### B. Proof of Lemma 2

Given the data collected from  $t-N$  to  $t$ , we prove Lemma 2 by forward induction in 3 steps. Step 1 proves the initial condition (17a) by considering the case of  $N = 1$ ; Step 2 shows that the key relation (36) holds for  $N = 2$ ; Step 3 shows that the key relation (36) holds for an arbitrary MHE horizon ( $N > 2$ ).

**Step 1** ( $N = 1$ ): Consider the simplest case where only the data at  $t - N$  is used and the auxiliary MHE system (16) reduces to a Kalman filter. The goal is to obtain the state estimate  $\hat{X}_{t-N|t-N}^{\text{KF}}$ . This can be achieved by solving the KKT condition (29a), which requires  $\hat{W}_{t-N|t-N}$  and  $\Lambda_{t-N}^*$ . Because there is no need to predict the system state, the KKT condition for the dynamics equality constraint (29d) can be removed and thus  $\Lambda_{t-N}^* = 0$ . It follows that we can express  $\hat{W}_{t-N|t-N}$  in terms of  $\hat{X}_{t-N|t-N}^{\text{KF}}$  from (29c) where  $k$  is set to be  $t - N$ . Plugging the resulting  $\hat{W}_{t-N|t-N}$  into (29a) and using  $\bar{X}_{t-N} = P_{t-N} T_{t-N} + \hat{X}_{t-N}$  yield

$$\hat{X}_{t-N|t-N}^{\text{KF}} = \bar{X}_{t-N} + P_{t-N} S_{t-N} \hat{X}_{t-N|t-N}^{\text{KF}}. \quad (30)$$

The above equation is equivalent to the following form:

$$\begin{aligned} (I - P_{t-N} S_{t-N}) \hat{X}_{t-N|t-N}^{\text{KF}} = & (I - P_{t-N} S_{t-N}) \bar{X}_{t-N} \\ & + P_{t-N} S_{t-N} \bar{X}_{t-N}. \end{aligned} \quad (31)$$

Define  $C_{t-N} = (I - P_{t-N} S_{t-N})^{-1} P_{t-N}$ . We can therefore simplify (31) to

$$\hat{X}_{t-N|t-N}^{\text{KF}} = (I + C_{t-N} S_{t-N}) \bar{X}_{t-N} \quad (32)$$

which is exactly the initial condition (17a).

**Step 2** ( $N = 2$ ): We move one step forward. Consider the case where the data at  $t - N$  and  $t - N + 1$  is used and the goal is to obtain the sequence  $\{\hat{X}_{t-N|t-N+1}, \hat{X}_{t-N+1|t-N+1}\}$ . From (29c), we solve for  $\hat{W}_{t-N|t-N+1}$  in terms of  $\hat{X}_{t-N|t-N+1}$  and  $\Lambda_{t-N}^*$ :

$$\begin{aligned} \hat{W}_{t-N|t-N+1} = & (L_{t-N}^{ww})^{-1} (G_{t-N}^T \Lambda_{t-N}^* \\ & - L_{t-N}^{wx} \hat{X}_{t-N|t-N+1} - L_{t-N}^{w\theta}). \end{aligned} \quad (33)$$

Using the above equation, we can rewrite (29a) as

$$\begin{aligned} \hat{X}_{t-N|t-N+1} = & \bar{X}_{t-N} + P_{t-N} S_{t-N} \hat{X}_{t-N|t-N+1} \\ & + P_{t-N} \bar{F}_{t-N}^T \Lambda_{t-N}^*. \end{aligned} \quad (34)$$

An equivalent expression similar to (31) can be obtained for (34). With  $C_{t-N}$  defined above, we can rewrite the equivalent expression of (34) as

$$\begin{aligned} \hat{X}_{t-N|t-N+1} = & (I + C_{t-N} S_{t-N}) \bar{X}_{t-N} \\ & + C_{t-N} \bar{F}_{t-N}^T \Lambda_{t-N}^*. \end{aligned} \quad (35)$$

Comparing with (32), we can reduce (35) to

$$\hat{X}_{t-N|t-N+1} = \hat{X}_{t-N|t-N}^{\text{KF}} + C_{t-N} \bar{F}_{t-N}^T \Lambda_{t-N}^*. \quad (36)$$

Note that we have  $\Lambda_{t-N+1}^* = 0$  as there is only one dynamics equality constraint associated with  $\Lambda_{t-N}^*$ . Using  $\Lambda_{t-N+1}^* = 0$  and (33), we can solve for  $\Lambda_{t-N}^*$  from (29b) as:

$$\Lambda_{t-N}^* = S_{t-N+1} \hat{X}_{t-N+1|t-N+1} + T_{t-N+1}. \quad (37)$$

Plugging (33) and (36) into the dynamics equality constraint (29d) yields the state prediction

$$\begin{aligned} \hat{X}_{t-N+1|t-N+1} = & \bar{F}_{t-N} \hat{X}_{t-N|t-N} \\ & - G_{t-N} (L_{t-N}^{ww})^{-1} L_{t-N}^{w\theta} \\ & + \bar{F}_{t-N} C_{t-N} \bar{F}_{t-N}^T \Lambda_{t-N}^* \\ & + G_{t-N} (L_{t-N}^{ww})^{-1} G_{t-N}^T \Lambda_{t-N}^*. \end{aligned} \quad (38)$$

Define

$$\hat{X}_{t-N+1|t-N} = \bar{F}_{t-N} \hat{X}_{t-N|t-N} - G_{t-N} (L_{t-N}^{ww})^{-1} L_{t-N}^{w\theta} \quad (39)$$

and

$$P_{t-N+1} = \bar{F}_{t-N} C_{t-N} \bar{F}_{t-N}^T + G_{t-N} (L_{t-N}^{ww})^{-1} G_{t-N}^T. \quad (40)$$

Using (39) and (40), we can rewrite (38) as

$$\hat{X}_{t-N+1|t-N+1} = \hat{X}_{t-N+1|t-N} + P_{t-N+1} \Lambda_{t-N}^*. \quad (41)$$

Plugging (37) into (41) yields

$$\begin{aligned} \hat{X}_{t-N+1|t-N+1} = & \hat{X}_{t-N+1|t-N} \\ & + P_{t-N+1} S_{t-N+1} \hat{X}_{t-N+1|t-N+1} \\ & + P_{t-N+1} T_{t-N+1}. \end{aligned} \quad (42)$$

After a procedure similar to the one used for (30), we can obtain an equivalent equation of (42) similar to (31). Let

$$C_{t-N+1} = (I - P_{t-N+1} S_{t-N+1})^{-1} P_{t-N+1}, \quad (43)$$

then we can simplify the equivalent equation of (42) to

$$\begin{aligned} \hat{X}_{t-N+1|t-N+1} = & (I + C_{t-N+1} S_{t-N+1}) \hat{X}_{t-N+1|t-N} \\ & + C_{t-N+1} T_{t-N+1}. \end{aligned} \quad (44)$$

Equations (36), (40), (43), and (44) are similar in structure to equations (20), (18b), (18c), and (18d) presented in Lemma 2, respectively. In particular, the relation (36) is the key to the general solution, as we will show shortly.

**Step 3** ( $N > 2$ ): Consider the general case where all the data in the horizon is used and the goal is to obtain the

complete sequence  $\left\{\hat{\mathbf{X}}_{k|t}\right\}_{k=t-N}^t$ . We aim to show that if (20) is satisfied by  $\hat{\mathbf{X}}_{k|t}$ , then it also holds for  $\hat{\mathbf{X}}_{k+1|t}$ . Before proceeding, first combine (29c) and (29d) to eliminate  $\hat{\mathbf{W}}_{k|t}$ :

$$\hat{\mathbf{X}}_{k+1|t} = \bar{\mathbf{F}}_k \hat{\mathbf{X}}_{k|t} - \mathbf{G}_k (\mathbf{L}_k^{ww})^{-1} \mathbf{L}_k^{w\theta} + \mathbf{G}_k (\mathbf{L}_k^{ww})^{-1} \mathbf{G}_k^T \boldsymbol{\Lambda}_k^*. \quad (45)$$

Similarly, after substituting  $\hat{\mathbf{W}}_{k|t}$  in (29b), we obtain

$$\boldsymbol{\Lambda}_{k-1}^* = \bar{\mathbf{F}}_k \boldsymbol{\Lambda}_k^* + \mathbf{S}_k \hat{\mathbf{X}}_{k|t} + \mathbf{T}_k. \quad (46)$$

Suppose that  $\hat{\mathbf{X}}_{k|t}$  satisfies (20) for  $k \in [t-N, t-1]$ . Then, from (45), we have

$$\begin{aligned} \hat{\mathbf{X}}_{k+1|t} &= \bar{\mathbf{F}}_k \hat{\mathbf{X}}_{k|k}^{\text{KF}} - \mathbf{G}_k (\mathbf{L}_k^{ww})^{-1} \mathbf{L}_k^{w\theta} \\ &\quad + \left[ \bar{\mathbf{F}}_k \mathbf{C}_k \bar{\mathbf{F}}_k^T + \mathbf{G}_k (\mathbf{L}_k^{ww})^{-1} \mathbf{G}_k^T \right] \boldsymbol{\Lambda}_k^*. \end{aligned} \quad (47)$$

Using (18a), we can simplify (47) to

$$\hat{\mathbf{X}}_{k+1|t} = \hat{\mathbf{X}}_{k+1|k} + \left[ \bar{\mathbf{F}}_k \mathbf{C}_k \bar{\mathbf{F}}_k^T + \mathbf{G}_k (\mathbf{L}_k^{ww})^{-1} \mathbf{G}_k^T \right] \boldsymbol{\Lambda}_k^*. \quad (48)$$

Substituting  $\mathbf{P}_{k+1}$  from (18b) and  $\boldsymbol{\Lambda}_k^*$  from (46), we obtain

$$\begin{aligned} \hat{\mathbf{X}}_{k+1|t} &= \hat{\mathbf{X}}_{k+1|k} + \mathbf{P}_{k+1} \mathbf{T}_{k+1} + \mathbf{P}_{k+1} \mathbf{S}_{k+1} \hat{\mathbf{X}}_{k+1|t} \\ &\quad + \mathbf{P}_{k+1} \bar{\mathbf{F}}_{k+1} \boldsymbol{\Lambda}_{k+1}^*. \end{aligned} \quad (49)$$

The above equation is equivalent to the following form:

$$\begin{aligned} (\mathbf{I} - \mathbf{P}_{k+1} \mathbf{S}_{k+1}) \hat{\mathbf{X}}_{k+1|t} &= (\mathbf{I} - \mathbf{P}_{k+1} \mathbf{S}_{k+1}) \hat{\mathbf{X}}_{k+1|k} \\ &\quad + \mathbf{P}_{k+1} \mathbf{S}_{k+1} \hat{\mathbf{X}}_{k+1|k} \\ &\quad + \mathbf{P}_{k+1} \mathbf{T}_{k+1} + \mathbf{P}_{k+1} \bar{\mathbf{F}}_{k+1} \boldsymbol{\Lambda}_{k+1}^*. \end{aligned} \quad (50)$$

Substituting  $\mathbf{C}_{k+1}$  from (18c) and  $\hat{\mathbf{X}}_{k+1|k+1}^{\text{KF}}$  from (18d), we obtain the desired relation as below:

$$\hat{\mathbf{X}}_{k+1|t} = \hat{\mathbf{X}}_{k+1|k+1}^{\text{KF}} + \mathbf{C}_{k+1} \bar{\mathbf{F}}_{k+1}^T \boldsymbol{\Lambda}_{k+1}^*. \quad (51)$$

This completes the proof.